Towards a High-Precision Atomic Gyroscope

by

Mackenzie A. Van Camp
B.A, Lawrence University (2009)

Submitted to the Department of Physics
in partial fulfillment of the requirements for the degree of
Master of Science in Physics
at the
MASSACHUSETTS INSTITUTE OF TECHNOLOGY
June 2013

Author . . .
Department of Physics
May 30, 2013

Certified by . . . .
Richard Stoner, Ph.D.
Distinguished Member of the Technical Staff, Charles Stark Draper Laboratory
Thesis Supervisor

Certified by . . . .
Vladan Vuletić, Ph.D.
Lester Wolfe Associate Professor of Physics
Thesis Supervisor

Accepted by . . . .
John Belcher, Ph.D.
Class of '22 Professor of Physics
Associate Department Head for Education

Towards a High-Precision Atomic Gyroscope

by

Mackenzie A. Van Camp

Submitted to the Department of Physics
on May 30, 2013, in partial fulfillment of the
requirements for the degree of
Master of Science in Physics

Abstract

In this thesis, I report on the design and construction of the **R**ubidium **A**tomic **G**yroscope **E**xperiment (RAGE) at Draper Lab.

Thesis Supervisor: Richard Stoner, Ph.D.
Title: Distinguished Member of the Technical Staff, Charles Stark Draper Laboratory

Thesis Supervisor: Vladan Vuletić, Ph.D.
Title: Lester Wolfe Associate Professor of Physics

Acknowledgments

To Vladan, for putting me on a new path.

To Rick, for pushing me to be the scientist I want to be.

To Brian, for sharing so much of his time and expertise.

To Dave J. for his scientific creativity, Dave B. for his guidance, Krish for making Draper feel like home, and Nicole and Marissa for sharing the master's experience with me.

To my wonderful interns Rob S. and Ilica. Can I keep you forever?

To Rob D. and Erik, who generously donated their copyediting skills.

To my dearest Kristina, who kept me sane. Love you, m'dear. See you at New Year's.

To Dave N., Lori, Zoe, Tyler, Pippin, and Ozzy. I love you all like family. Thank you for taking us in.

To Miri, thank you. *Light! More light! Veritas est Lux.*

To my dad for giving me his love of science, my brother for always understanding, and my mother for making me ask questions.

And most of all, to Rob Z. We made it.

Love,
Mackie

This thesis was prepared at the Charles Stark Draper Laboratory, Inc., under the Internal Research and Development Program. Project ID 26353 Activity ID 001 and Project ID 27606 Activity ID 001.

Publication of this thesis does not constitute approval by Draper or the sponsoring agency of the findings or conclusions contained herein. It is published for the exchange and stimulation of ideas.

Mackenzie A. Van Camp

Assignment

Draper Laboratory Report Number T-1748.

In consideration for the research opportunity and permission to prepare my thesis by and at The Charles Stark Draper Laboratory, Inc., I hereby assign my copyright of the thesis to The Charles Stark Draper Laboratory, Inc., Cambridge, Massachusetts.

Mackenzie A. Van Camp Date

THIS PAGE INTENTIONALLY LEFT BLANK

Contents

List of Figures

List of Tables

THIS PAGE INTENTIONALLY LEFT BLANK

Chapter 1

Introduction

1.1 Motivation for high-precision inertial sensors

With a GPS receiver in nearly every modern cell phone, the need to navigate via maps and landmarks can seem a little old fashioned. But what if GPS isn't available? What if communication is insecure, unreliable, or simply physically impossible? That is the niche that self-contained inertial sensors fill.

Inertial sensors track position by monitoring acceleration or rotation. Position is determined by integrating the rotation and acceleration signals and analyzing the results in conjunction with an onboard map of local gravity. A full inertial measurement unit (IMU) monitors all three axes of acceleration and rotation. With an IMU, if you know where started, you know where you are, with no need for GPS or other external references.

Given the equivalence principle, high-precision inertial sensors can also be used for gravimetry and geodesy. At high enough precision, they can be tools for tests of general relativity and geophysical surveying.

1.2 Introduction to inertial sensors

This section gives an overview of modern accelerometer and gyroscope technology. This is not a comprehensive overview; rather, it describes a few devices that concisely illustrate the motivation for this thesis.

1.2.1 Accelerometers

The Pendulous Integrating Gyroscopic Accelerometer (PIGA) has an uninterrupted line of development from the V2 to modern ballistic missiles. Its debut in the V2 was the first practical use of an inertial navigation system, and modern PIGAs remain the benchmark for mechanical accelerometer performance under high dynamic range conditions [6].

Mechanical accelerometers, though, suffer high production costs, exacting manufacturing requirements, and performance decay over time due to wear. PIGAs also are not capable of the sensitivity necessary for longer duration missions where small drifts and imprecisions have time to integrate to unacceptable position errors. These problems motivate the development of new inertial sensing technologies that are simpler to manufacture, have no moving parts and longer lifetimes, and are capable of much higher precision than the current generation of mechanical inertial sensors.

A relatively new inertial sensing modality is light pulse atom interferometry (LPAI). LPAI leverages the wave-like properties of matter to measure inertial changes with extremely high precision. The Stanford long baseline accelerometer showcases the exquisite precision that atomic inertial sensors are capable of. Currently under construction, it will measure the Weak Equivalence Principle to a part in 10^{-15} [7]. At $8.8m$ long, it's hardly a compact device, but it illustrates the power of LPAI for inertial sensing.

Not all atom interferometers are as large or fragile as the long baseline accelerometer. Some recent developments in atom optics focus on improving the sensitivity and robustness of atom interferometers. This advance allows greater precision in small ($< 100cc$) volumes and enhances the ability of atom interferometers to perform in highly dynamic environments [8–10].

1.2.2 Gyroscopes

An example of the extreme precision possible with mechanical gyroscopes is Gravity Probe B (GPB), a satellite in operation from 2004-2005 with the mission of measuring frame-dragging and the geodetic effect. Spherical to within 40 atoms, the superconducting GPB proof mass was suspended by electric fields and the precession was measured by its London moment [11]. The predicted magnitude of the geodetic effect was confirmed to within 0.3%,

and frame-dragging to within 19% [12].

Mechanical gyroscopes, however, are vulnerable to the same problems as mechanical accelerometers. For many applications, they are being replaced with all-optical gyroscopes with no moving parts. Fiber Optic Gyroscopes (FOGs) measure the difference in phase accumulated by counterpropagating beams in a long loop of fiber. FOGs are also very physically robust and can be "hardened" against the effects of radiation [6].

The advantages that make atom interferometers appealing for next-generation accelerometers also make them strong candidates as gyroscopes. In 2000, Gustavson and coworkers demonstrated an atom interferometer gyroscope with $6E-10\text{rad/s}$ precision when integrated for one second [13].

1.2.3 Precision measurement

One of the key postulates of general relativity is the equivalence principle; *i.e.*, that acceleration and gravitational forces are indistinguishable in any reference frame. Thus accelerometers can also be used as gravimeters. Ultra-high precision gyroscopes – like Gravity Probe B – can also be used to measure General Relativistic effects like frame dragging and the geodedic effect. Cold atom inertial sensor modalities, in particular, have potential applications for both guidance and fundamental science.

1.2.4 Performance specifications

Three factors bear centrally on accelerometer and gyroscope performance: sensitivity, scale factor stability, and bias stability.

Sensitivity is a measure of the short-timescale performance capabilities of the device. This is reported in terms of random walk: velocity random walk measured in units of $g/\sqrt{Hz}$ for accelerometers, and angle random walk in units of $deg/\sqrt{hr}$ for gyroscopes.

Scale factor is the ratio of the output signal (usually a voltage) to the quantity being measured. While a higher scale factor is generally preferable, more important is the *stability* of the scale factor over time, as variations will result in misinterpretation of the raw signal. Scale factor stability is typically reported in ppm.

Thanks to MEMS technology, most people encounter accelerometers and gyroscopes every

Table 1.1: Characteristic performance metrics of inertial sensors in the highest performance class for flight navigation systems [1].

Sensor Metrics	*100 m/hr*	*5 m/hr (Future)*
Accelerometer		
Sensitivity ($\mu g/\sqrt{\text{Hz}}$)	50	2
Bias stability (μg)	1	< 0.1
Scale factor stability (ppm)	1-10	<0.1
Gyroscope (strapdown)		
Sensitivity (mdeg/$\sqrt{\text{hr}}$)	0.1	<0.05
Bias stability (mdeg/hr)	0.5	<0.02
Scale factor stability (ppm)	1-10	<0.1
Size, weight, and power		
Volume (cc)	100-600	Similar
Power (W)	5-35	Similar
Weight (g)	300-2200	Similar

day in their cell phones or gaming devices. As a relatable basis for comparison, cell phone MEMS gyroscopes have a sensitivity on the order of $0.01 deg/\sqrt{s}$ and scale factor stability of 4% [14]. Bias stability is not typically reported, since the on-board inertial sensors are only used to detect the user's manipulation of the phone. Navigation is handled by the GPS system.

Atomic inertial sensors vary in their bias stability, but can offer extremely high precision. When paired with a MEMS device or other system for correcting bias drifts, they can offer excellent performance for scientific and navigation applications. The Rubidium Atomic Gyroscope Experiment (RAGE) is designed to be capable of $30 nanodeg/\sqrt{\text{hr}}$ sensitivity when operated in the Bragg LPAI regime (see section 2.2.2). The initial purpose of RAGE is to push the precision limits of atomic inertial sensors, not the bias stability.

1.3 Atomic inertial sensors

With the experimental realization of atom-wave interferometry in 1991, the door opened for a new regime of interferometric sensors [15–17]. Broadly speaking, atom-wave interferometry is a direct analog of optical interferometry, with the advantage that atom wave response to inertial effects is stronger than light wave phase response by roughly the ratio of the atom rest energy to the photon energy, around 10^{10} [1,18]. This leads to a much larger accumulation of

phase for a given inertial input, resulting in sensitivity that is orders of magnitude higher. In practice, the difference in sensitivity is less than 10^{10}: optical interferometers typically enclose much more area and have many more effective proof-masses than atom interferometers, giving optical sensors a boost in SNR. Even so, a potential net sensitivity advantage of several orders of magnitude could be realized by atom inertial sensors.

1.3.1 Overview of thesis

The subject of this thesis is the design and construction of the **R**ubidium **A**tomic **G**yroscope **E**xperiment (RAGE), an ultra-high precision cold atom inertial sensor. While RAGE is ultimately intended for use as a ultra-cold atom gyroscope, its design also permits versatile operation as an accelerometer and gravimeter in two different atom interferometry modalities.

This thesis is organized as follows:

- Ch2: Light Pulse Atom Interferometry
- Ch3: RAGE Design
- Ch4: Experimental Apparatus
- Ch5: Preliminary Results
- Ch6: Conclusion

THIS PAGE INTENTIONALLY LEFT BLANK

Chapter 2

Light-Pulse Atom Interferometry

This section summarizes the core physics concepts in RAGE: light-pulse atom interferometry (LPAI), and magneto-optical cooling and trapping of atoms.

2.1 Introduction to LPAI inertial sensors

2.1.1 LPAI as an analog of optical interferometry

A simple optical interferometer is constructed of two basic elements: mirrors and beamsplitters. Mirrors change the direction of the beam, and beamsplitters split or combine beams. A light-pulse atom interferometer works on the same principle, but the mirrors and beamsplitters are replaced with pulses of laser light [18].

In LPAI, atoms are prepared in the ground state and then spatially separated and recombined by a sequence of pulses from counterpropagating lasers. Different phase is accumulated by the atoms along each path depending on inertial effects, and the inertial effects are read out in the population difference of the states of the atoms at the output of the interferometer. The analog of a mirror is a π-pulse, which inverts the population balance. The role of the beamsplitter is played by a $\pi/2$-pulse, which takes a pure state into a balanced coherent superposition and vice-versa (see figure 2-1).

For both gyroscopes and accelerometers, the precision increases with the area enclosed by the interferometer. The area can be increased by either increasing the dwell time between pulses or by adding more pulses. Increasing the dwell time is only useful as long as you're

well below the coherence time of the atomic superposition, otherwise any nominal gains in precision are obliterated by loss of contrast in the final interferogram.

2.1.2 LPAI gyroscopes and accelerometers

LPAI gyroscopes and accelerometers work by measuring the phase acquired by each arm of the interferometer as the cold atom cloud is displaced by inertial input. Figure 2-2a) and b) illustrate the effects of acceleration and rotation on the cold atom cloud, respectively. With a single cloud, however, is is impossible to separate the effects of rotation and acceleration on the interferometer. Figure 2-2c) illustrates a two-cloud configuration that can distinguish between the effects of rotation and acceleration by throwing a pair of clouds at each other.

2.2 LPAI modalities: Bragg and Raman interferometry

This section will focus on two LPAI modalities: Raman and Bragg.

The primary difference between the two is that Raman beamsplitter pulses change both the internal and the momentum state of the atoms, while Bragg pulses only change the momentum state. Bragg interferometry thus avoids certain systematic errors encountered in Raman interferometry (see below), but the trade-off is that Bragg has stricter requirements for vacuum pressure and atom temperature.

2.2.1 Raman LPAI

The Raman LPAI modality is commonly used in state-of-the-art light-pulse atom interferometers, and will provide an excellent method for characterizing some of the improvements that RAGE offers over other similar apparatuses. Raman LPAI is also a direct analog of magnetic resonance imaging, which provides sophisticated techniques for interferometers beyond the simple three-pulse system described above.

In Raman LPAI, a pair of counterpropagating laser beams are used to drive a two-photon stimulated Raman transition between ground states of an atom. This is illustrated in figure

2-3. The atom acts as an intermediary to transfer energy from one field to the other, picking up the extra $2\hbar k$ of momentum in the process.

Raman LPAI has relatively forgiving technical requirements. Since the resonance condition is determined by the *difference* in frequency between the beams, an $\mathcal{O}(1MHz)$ linewidth laser is perfectly adequate. Traditional Raman LPAI can only transfer $2\hbar k$ of momentum per π pulse. Additional augmentation pulses can be applied to achieve larger momentum transfer and higher sensitivity [8, 19].

The details of Raman LPAI are discussed in references [20–23]. A semi-classical treatment is given in [1].

2.2.2 Bragg LPAI

Bragg LPAI imposes more stringent technical requirements than Raman, but offers benefits for LMT interferometry. Since we want RAGE to be capable of operating in both regimes, the design is based on Bragg LPAI prerequisites. The design is discussed in more detail in Chapter 3.

Like Raman LPAI, Bragg LPAI is rooted in a two-photon process driven by counterpropagating laser beams. With Bragg scattering, however, the photons impart momentum to the atom without changing the internal state. This is illustrated in figure 2-4.

Keeping the atoms in the same internal state throughout the interferometer imparts many benefits. Since the internal state doesn't change, the beams can be tuned to impart many $\hbar k$ of momentum in a single pulse. Furthermore, all state-dependent phase shifts (Stark, Zeeman, etc) become common mode. These processes are a major source of contrast loss in Raman interferometers.

These benefits, however, come at a cost. The atoms must be extremely cold in order to move slowly enough to prevent thermal motion from overwhelming the effects of Bragg scattering, and then even colder to reduce uncertainty in the initial velocity of the atoms and achieve our $30 nanodeg/\sqrt{\text{hr}}$ sensitivity goal. This requires a temperature below $10nK$ [24]. The atom proof mass must therefore be a Bose-Einstein Condensate (BEC).

The details of Bragg scattering and Bragg LPAI are discussed in references [24–26].

2.3 Cooling and trapping

The LPAI techniques described above share an important base requirement: a cloud of atoms cold enough to maintain coherence over the interrogation time of the interferometer. We create a cold atom cloud with a standard 3D magneto-optical trap (3D MOT) as described in [27]. To meet the lower temperature requirements for Bragg LPAI, we will evaporatively cool in a magnetic trap and a far-off-resonant optical trap. [28].

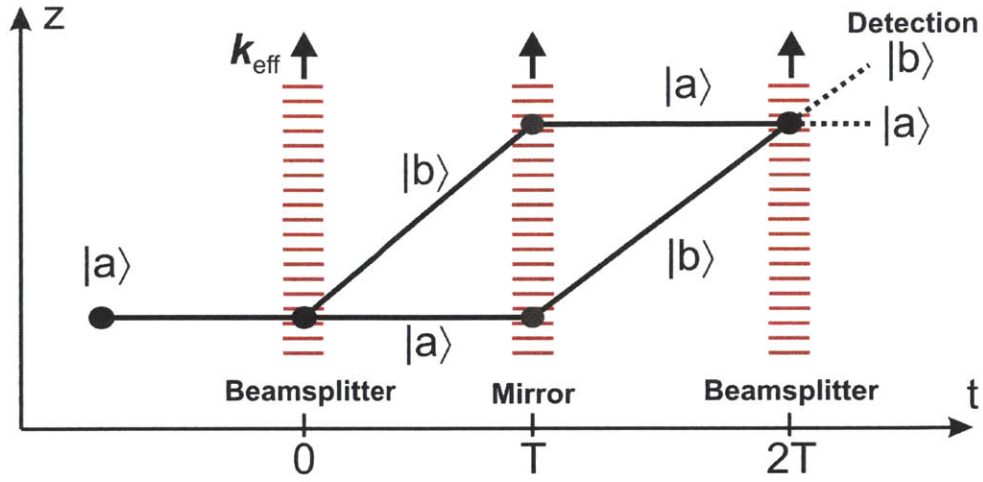

Figure 2-1: Diagram of three-pulse LPAI. Adapted from [1].

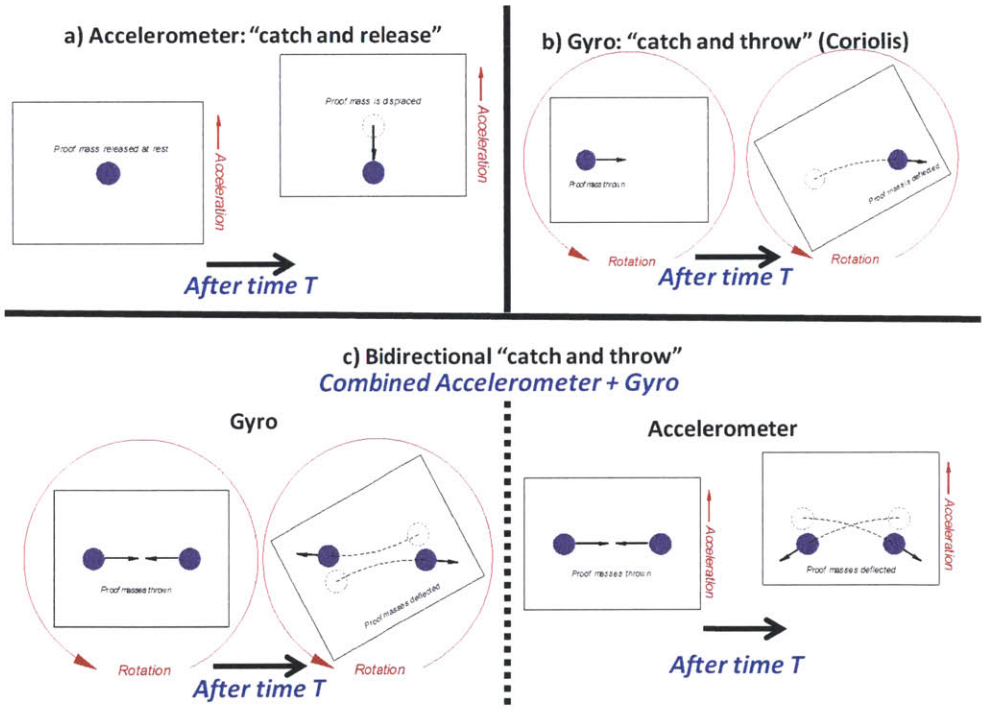

Figure 2-2: Illustration of a) accelerometer, b) gyroscope, and c) hybrid LPAI configurations

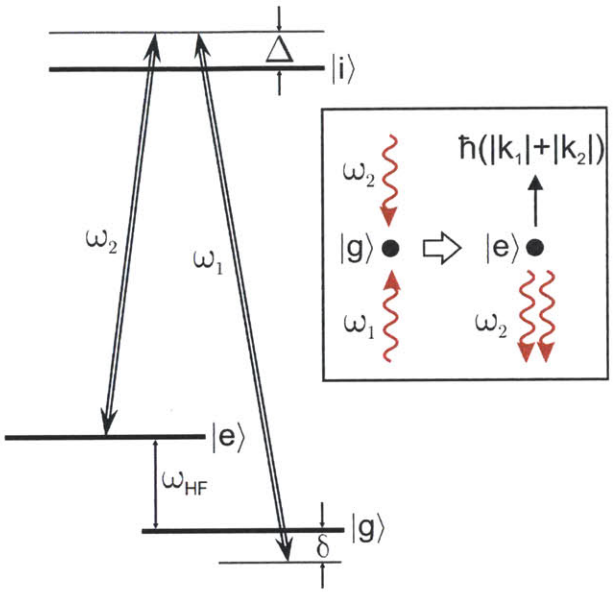

Figure 2-3: Diagram of a stimulated Raman transition.

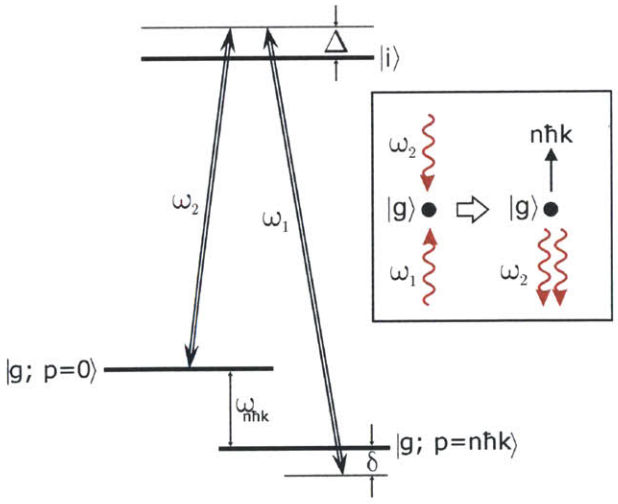

Figure 2-4: Diagram of a stimulated Bragg transition.

Chapter 3

RAGE Design

This chapter describes the ultimate design of RAGE. Since Bragg diffraction has more stringent requirements than Raman, it motivates most of the design decisions.

3.1 Requirements for Bragg

As described in the previous chapter, Bragg LPAI requires ultracold atoms. In order to minimize dephasing collisions, the background pressure of the 3D vacuum chamber must be extremely low, ideally on the order of $1E-11$ torr.

It is also desirable to detune the Bragg beams as far as possible from atomic resonance to reduce spontaneous emission. This is possible so long as the laser power is increased commensurately to maintain the Rabi rate. Thus RAGE requires a laser system that is very high power.

3.2 Cold atom proof mass

This section describes our design of the cold atom proof mass. For Raman LPAI, the proof mass is a 3D MOT loaded from a 2D MOT. For future Bragg LPAI operation, additional cooling and trapping steps will be used to evaporatively cool the MOT to a BEC.

3.2.1 2D MOT atom source

The vacuum requirements immediately place constraints on the atom source design. Placing a rubidium source in the main chamber would result in the accumulation of metal on the chamber walls, creating a background pressure above our requirements. Furthermore, the rubidium-rubidium scattering cross section is significantly higher than the rubidium-hydrogen cross section, so a small increase in background pressure due to rubidium is much more damaging than an increase due to hydrogen leakage.

Loading the MOT from thermal atoms is also inefficient. It is preferable to have an initial pre-cooling stage, which allows for faster MOT loading and ultimately higher repetition rates in the interferometer.

Both requirements are met in RAGE by using a 2D MOT to create a pre-cooled beam of atoms. This beam is directed at the center of the primary MOT trapping region to maximize capture efficiency and protect the fidelity of the ultra-high vacuum. Another advantage is that the 2D MOT acts as an isotopic filter: we use natural abundance rubidium, but only the trapped species is delivered to the 3D MOT.

2D MOTs are a compact, versatile alternative to Zeeman slowers for creating a cold beam of atoms. Our 2D MOT design is based on Ref. [2]. It operates on the same cooling and trapping mechanics as a 3D MOT, but leaves one axis unconfined. This results in the atoms being cooled in two dimensions and flowing along the free axis.

Given the results of [2], we expect to saturate the atom flux at 74mW with a 1-inch diameter beam at a 1:1 aspect ratio.

3.2.2 3D MOT

3.2.3 Evaporative cooling to BEC

We opt to cool our atoms to a BEC in a far-off-resonant optical trap (FORT). We will initially cool in the MOT, then turn off the trapping light and ramp up the magnetic trap coils to begin evaporative cooling. This configuration is essentially an "unplugged" plugged optical trap [29]. We will then confine the atoms in a 25W, 1064nm far-off-resonant trap where the atoms will be further cooled to a BEC.

3.3 780nm laser system

To avoid the complication of injection or phase locking multiple lower-powered lasers, it is preferable that all 780nm light in the experiment come from a single source. While multi-Watt 780nm laser systems are not commercially available, it it possible to construct a high-power, 780nm laser system via a telecom laser and second harmonic generation in a nonlinear crystal.

Nonlinear optical effects occur when the polarization density of a material is nonlinear in E:

$$\vec{\mathbf{P}}(t) = \epsilon_0(\chi^{(1)}\vec{\mathbf{E}}(t) + \chi^{(2)}\vec{\mathbf{E}}^2(t) + \chi^{(3)}\vec{\mathbf{E}}^3(t) + ...) \tag{3.1}$$

Second-order nonlinear materials, specifically, have a polarization that is quadratic in $\vec{\mathbf{E}}$. For simplicity, we refer to the quadratic term as $\vec{\mathbf{P}}^{NL}(t)$. If we take $\vec{\mathbf{E}}$ to have two frequency components

$$\vec{\mathbf{E}}(t) = \vec{\mathbf{E}_1}e^{-i\omega_1 t} + \vec{\mathbf{E}_2}e^{-i\omega_2 t} + c.c, \tag{3.2}$$

then we can expand the second order polarization in terms of each frequency:

$$\vec{\mathbf{P}}^{NL}(t) = \epsilon_0\chi^{(2)}\vec{\mathbf{E}}^2(t)$$
$$= \epsilon_0\chi^{(2)}[|\vec{\mathbf{E}_1}|^2e^{-i2\omega_1 t} + |\vec{\mathbf{E}_2}|^2e^{-i2\omega_2 t} + 2E_1E_2e^{-i(\omega_1+\omega_2)t} + 2E_1E_2^*e^{-i(\omega_1-\omega_2)t} + 2(|\vec{\mathbf{E}_1}| + |\vec{\mathbf{E}_2}|)]. \tag{3.3}$$

Thus second-order nonlinearities can drive fields at $2w_1$, $2w_2$, w_1+w_2, w_1-w_2, and 0 (second harmonic generation, sum and difference frequency generation, and optical rectification). The three processes with nonzero frequency are illustrated in 3-3.

With a source at 1560nm, second harmonic generation will produce a beam at 780nm. A common material for second harmonic generation in the telecom band is lithium niobate, a crystal with a strong $\chi^{(2)}$ interaction.

The crystal structure is "poled" to optimize the efficiency of the second harmonic generation. Without poling, 780nm photons would be produced incoherently throughout the crystal. Interference would result in a very low net conversion efficiency. By periodically alternating the direction of the crystalline structure, the 780nm photons are kept roughly in

phase with the 1560nm drive light. This is a form of quasi-phase matching, and it builds the 780nm power coherently throughout the crystal (figure 3-4).

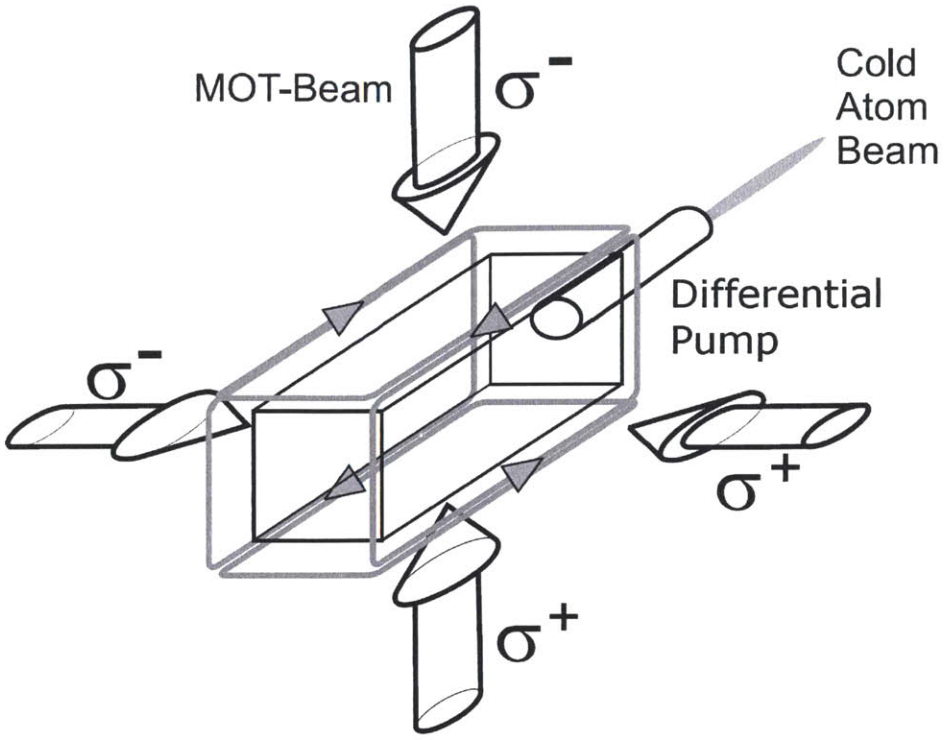

Figure 3-1: Schematic view of the 2D MOT system. Adapted from [2].

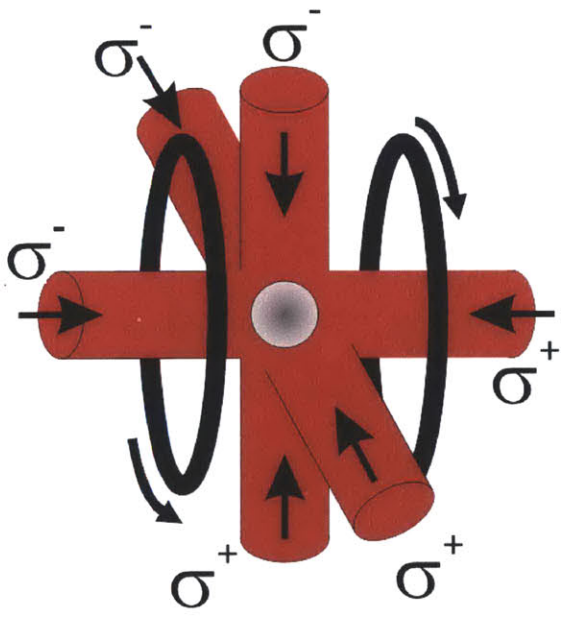

Figure 3-2: Schematic of the 3D MOT. Adapted from [1].

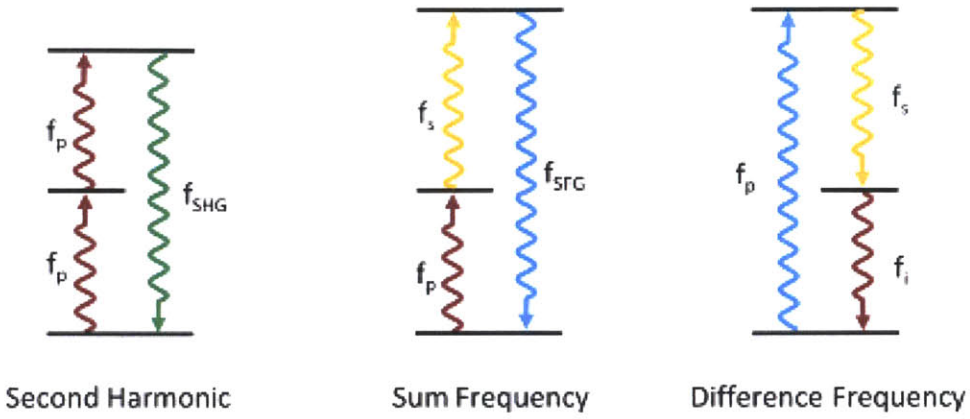

Figure 3-3: Second-order nonlinear interactions. From left to right: second harmonic generation, sum frequency generation, and difference frequency generation. Adapted from [3].

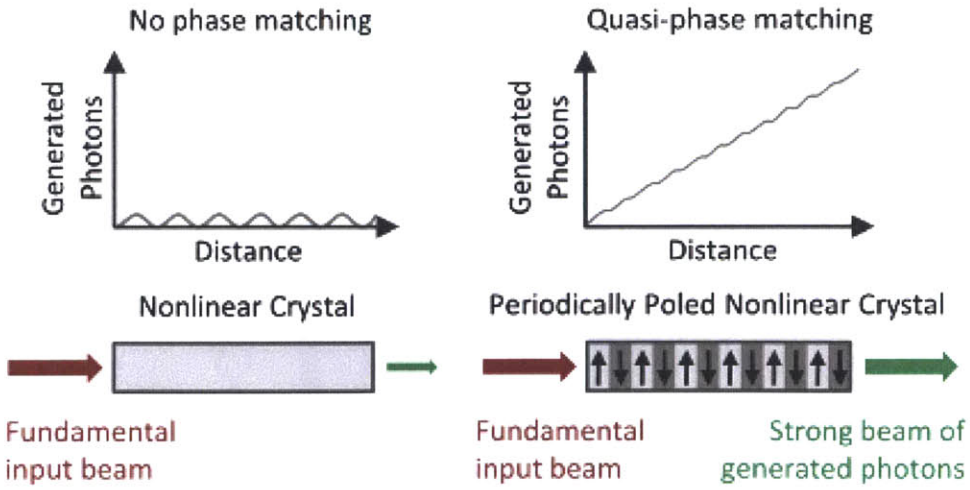

Figure 3-4: Illustration of quasi-phase matching. Adapted from [3].

Chapter 4

Experimental Apparatus

4.1 Goals for experimental work

The primary goals of this thesis are to:

- Construct a laser system capable of powering a Bragg LPAI BEC gyroscope.
- Construct a ultra-high vacuum system with pressures low enough for ultra-high precision inertial sensing.
- Create a 2D MOT cold atom source.
- Load a 3D MOT from the 2D source.

The remainder of the system – such as the interferometry beams, and the evaporative cooling system – will be installed in the coming months. The entire apparatus was constructed by the author, with assistance from interns for the electronics and staff for the MOT optimization.

4.2 Overview of the apparatus

RAGE currently consists of a single high-power 780nm laser system that provides cooling and repump light to the entire system, a 2-part vacuum chamber with UHV on the 3D MOT (and future atom interferometry) side and HV on the 2D MOT side separated by a differential pump, and the 2D and 3D MOT optical and electronic systems.

While we will ultimately do interferometry with ^{87}Rb, the initial setup was done with ^{85}Rb. The rubidium in the chamber is natural abundance, so the ^{85}Rb signals are significantly stronger and easier to work with for preliminary tasks like MOT alignment. In the future we will switch to ^{87}Rb operation by adding a frequency offset via AOM. It is much simpler to form a BEC with ^{87}Rb because it has a positive scattering length; ^{85}Rb has a negative scattering length below its Feshbach resonance, which adds additional complexity to forming a BEC with that isotope [30, 31].

4.3 Laser system

In order to achieve the laser power requirements in section 2.2.2, a total of $5W$ of laser power is required.

In particular, a 1560nm RIO GRANDE pigtailed laser module seeds an IPG Photonics Erbium-doped fiber amplifier (EDFA) produces up to 20W at 1560nm. With proper focusing through a periodically poled lithium niobate crystal (PPLN), a 20W 1560nm beam can be frequency doubled to 780nm with nearly 25% efficiency. The frequency doubling efficiency is linear in input power. It is also relatively inexpensive to acquire a narrow-linewidth telecom laser, so we opt for the $3.6kHz$ linewidth model. This will ultimately provide benefits in inertial sensor stability in the Bragg regime.

4.3.1 Offset lock

For the initial construction phase of RAGE, every beam is used for cooling and trapping the atoms. It is convenient to lock the laser at 10MHz to the red of the $F = 3 \rightarrow F' = 4$ cooling transition so the light can be sent directly to the MOTs.

A quick examination of figure 4-2 suggests the $F = 3 \rightarrow F' = 2x4$ crossover transition as a promising lock point. It is the strongest feature on the rubidium D2 line in either isotope, and differentiating the signal would provide a steep zero-crossing at the peak of that feature. This allows robust locking of the laser to a well-defined frequency landmark.

The separation between the $2x4$ crossover and the cooling transition is 82.2MHz, well within range of a standard AOM. We pass the dump light from the high-power polarizing beamsplitter cube shown in 4-1 through an AOM to apply this offset. The differentiated

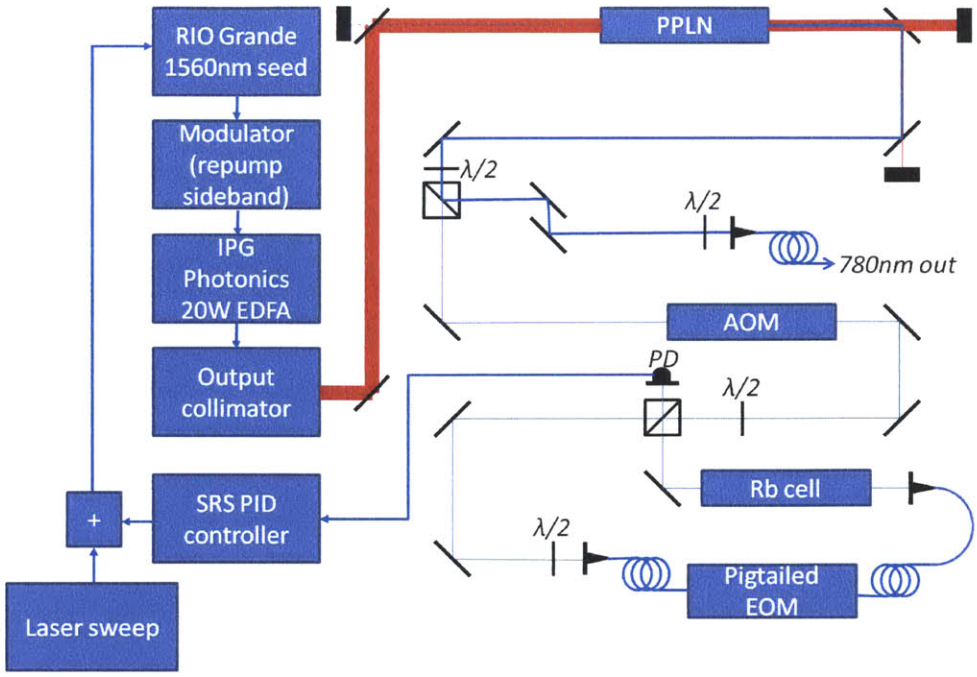

Figure 4-1: Schematic of the laser system.

error signal is produced by modulating one arm of a saturated absorption spectroscopy setup at 10MHz, then demodulating the saturated absorption signal with the RF circuit shown in 4-3. Locking the laser at the zero of the frequency offset differentiated $2x4$ crossover puts the main beam at the desired frequency, 10MHz to the red of the $F = 3 \rightarrow F' = 4$ transition.

Closed-loop operation is achieved via a SRS PID controller, which is summed with the laser current sweep for convenience.

4.3.2 Repump sideband

By the same argument as above, it makes sense to have the $F = 2 \rightarrow F' = 3$ repump light be a sideband on the cooling light. It is convenient to place the sideband on the 1560nm light with a pigtailed JDS Uniphase modulator placed between the seed and the amplifier. Since the sideband is generated before the light is frequency-doubled in the PPLN, the modulator must be set at half the ground state separation of ^{85}Rb (1.462546GHz) [5]. Driving the modulator at $30dBm$ places 10% of the light in the repump sideband. The laser frequencies are illustrated in figure 4-4.

4.4 Vacuum system

The vacuum is maintained by a system of four pumps. Both the 2D and 3D MOT sides of the chamber have a SAES getter pump housed in a 2.75" nipple. The 3D chamber has a $35l/s$ Gamma Vacuum ion pump, and the 2D chamber has a $2l/s$ Thermionics ion pump.

The 2D and 3D chambers are separated by a differential pump capable of maintaining a $100x$ pressure differential. There are also four valves in the system: one valve each on the 2D and 3D for attaching a roughing hose, a valve to isolate the nipple containing the solid rubidium, and a gate valve between the Rb and roughing assembly on the 2D and the rest of the chamber. These are visible in figure 4-5.

The chamber is roughed out with an Agilent turbo pump to $1E-7$ torr. With the turbo pump still attached, the chamber is then wrapped in heating tape and foil and baked for 4 days at 180C. The SAES rubidium sources are also activated at this time per the method described in reference [1], and the two getter pumps are activated by running at 4A for an hour.

At this point the nipple containing the rubidium is crushed to break the ampoule so the nitrogen could be pumped away. It is crucial to wait to crush the ampoule until after the bake-out so that residual moisture in the nipple does not oxidize any of the rubidium.

Once the nitrogen is pumped away, the turbo pump is valved off from the chamber and disconnected and the ion pumps are activated.

4.5 2D MOT atom source

4.5.1 2D optics

A challenge with our 2D MOT system is the mechanical stability of the optics. Since the 2D chamber is well above the table and at an odd angle, it isn't feasible to mount the optics from the tabletop. Instead, we bolt a support plate to the top window of the 2D chamber to support cage-mounted optics. An aluminum plate over each coil anchors the end of each set of cage rods. The entire 2D chamber is also braced by a rail bolted to the support plate.

Due to the sensitivity of 2D MOTs to light force imbalances, it is not possible to operate with retroreflected beams. Nearly 15% of the power is absorbed in a single pass through the

2D MOT chamber, and the resulting light force imbalances in the counterpropagating beam pairs would drive the atoms out of the trapping region. Four separate collimators are used to convey the 2D MOT light to the trapping region.

4.5.2 2D coils

The 2D MOT has four rectangular coils: two for trapping, and two for field zero adjustment. All four coils have 100 turns of 17 gauge square cross-section magnet wire.

The main coils are anti-aligned and separated by $2.975in$, and each is controlled by a 760W power supply capable of sourcing 19A. A 5A current in each coil will produce a $15G/cm$ magnetic field gradient.

The bias coils are aligned and wired in parallel. The pair is controlled by one of the outputs of a 20W, 4-channel power supply capable of sourcing 6A.

4.5.3 SAES backups

The primary implementation challenge of the 2D MOT system is that it is very sensitive to alignment compared to a 3D MOT, since the 2D MOT only cools along two axes. Light force imbalances due to power or polarization mismatches impart a transverse velocity that pushes the atoms out of the trapping region.

Somewhat perversely, one of the easiest ways to optimize the 2D MOT is to measure how well it loads the 3D MOT. This requires that the 3D MOT be properly aligned *before* the 2D atom source is constructed. To circumvent this problem we have two 12mm SAES solid-state rubidium sources in the main chamber, a primary and an emergency backup. While the previously stated concerns about dirtying the main chamber still hold, that might become a concern over many days or weeks of operating a rubidium source. Little damage is done by briefly running the SAES sources to align the 3D MOT fields. The pressure increases to $1E-8$ torr while the sources are running, but returns to $5E-10$ torr within a few days. The SAES sources are no longer used once the 3D MOT is aligned and successfully being loaded by the 2D MOT.

4.6 3D MOT

4.6.1 3D main coils

The primary anti-Helmholtz coils on the 3D MOT are each constructed of 20 turns of 0.125 inch wide square cross-section copper wire with a 0.06 inch diameter hollow core. The clear aperture about the axis of each coil is 1.55 inches, and they are separated by about 4 inches. Figure 4-7 shows a photograph of the coils in the partially-assembled vacuum chamber. The coils are serving double-duty as the MOT coils and the magnetic trapping coils for the initial evaporative cooling stage. Thus they must be inside the chamber and capable of operating at high current to provide a steep enough field gradient for evaporative cooling.

In order to achieve the highest repetition rate possible in the interferometer, it is necessary to rapidly power up and power down the coils. Since the coils are very large inductors, this requires ringing the power in and out of large capacitors. The coils will ultimately be run at up to 200 A, so the switching circuit must be capable of handling multiple Watts of power. The final design of the circuit is shown in figure 4-8. The circuit is built and has been tested in DC operation at up to 5A. We are currently wary of running at higher currents due to the limiter cooling power of our water chiller. A replacement chiller should allow operation up to 200A. The switching time is predicted to be sub-microsecond.

Operating at high current also mandates a cooling system for the coils. The coils are insulated with kapton, which breaks down around 400C. A chiller is necessary to prevent the kapton insulation on the coils from decomposing and shorting the turns together.

Water and current are carried to the coils via four custom ceramic-insulated power and water feedthroughs manufactured by MPF Products, Inc, shown in figure 4-7. An initial attempt was made to modify a stock ceramic/metal feedthrough by brazing on the necessary connectors in-house, but this resulted in small cracks in the ceramic which were not apparent until our first attempt to pump down the chamber stalled at $1E-6$ torr.

4.6.2 3D trim coils

Each of the 3D MOT trim coils has 100 turns of 17 gauge square cross-section copper magnet wire wound on a round delrin frame. The coils are mounted to the vacuum chamber via

aluminum braces (see figure 4-9). The x, y, and z coils have clear aperture of 8.25, 8.25, and 16.85 inches, respectively. Each axis's coils are wired in parallel and powered by one of the outputs of the 6A supply mentioned in section 4.5.2.

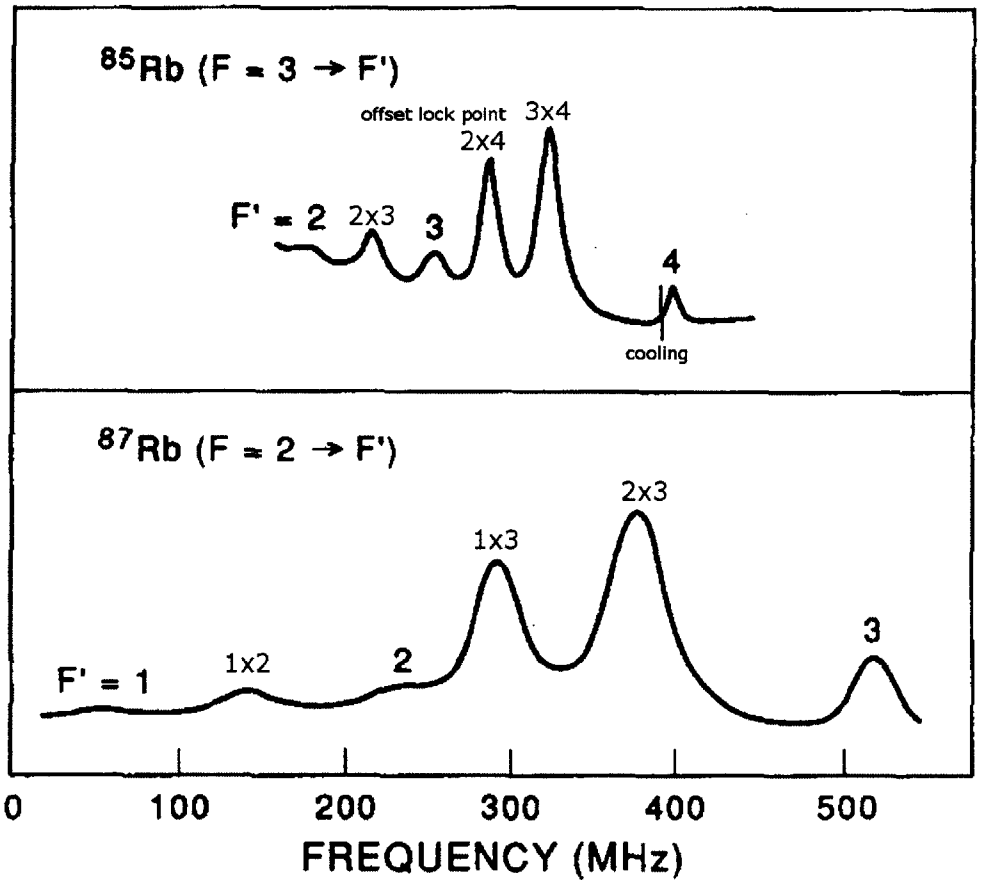

Figure 4-2: Doppler-free spectrum of the rubidium D2 line in arbitrary units. Adapted from [4].

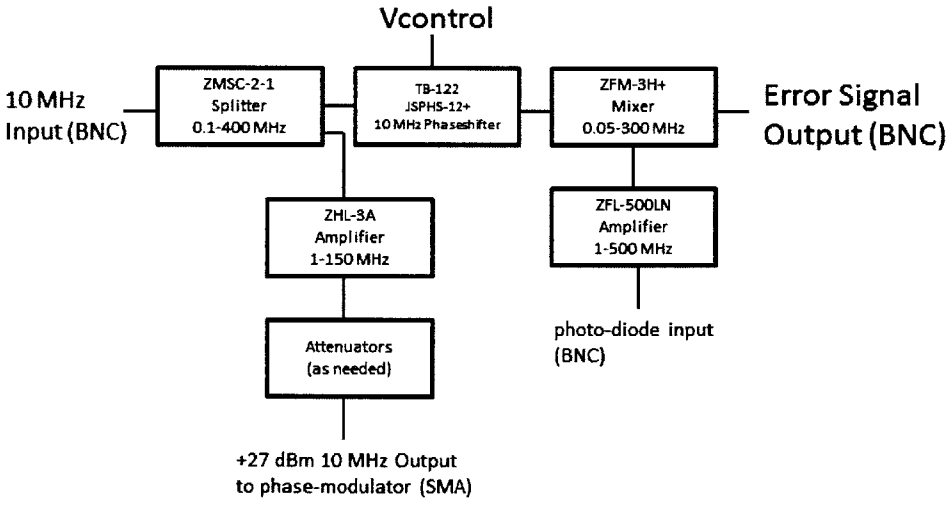

Figure 4-3: Offset lock RF electronics.

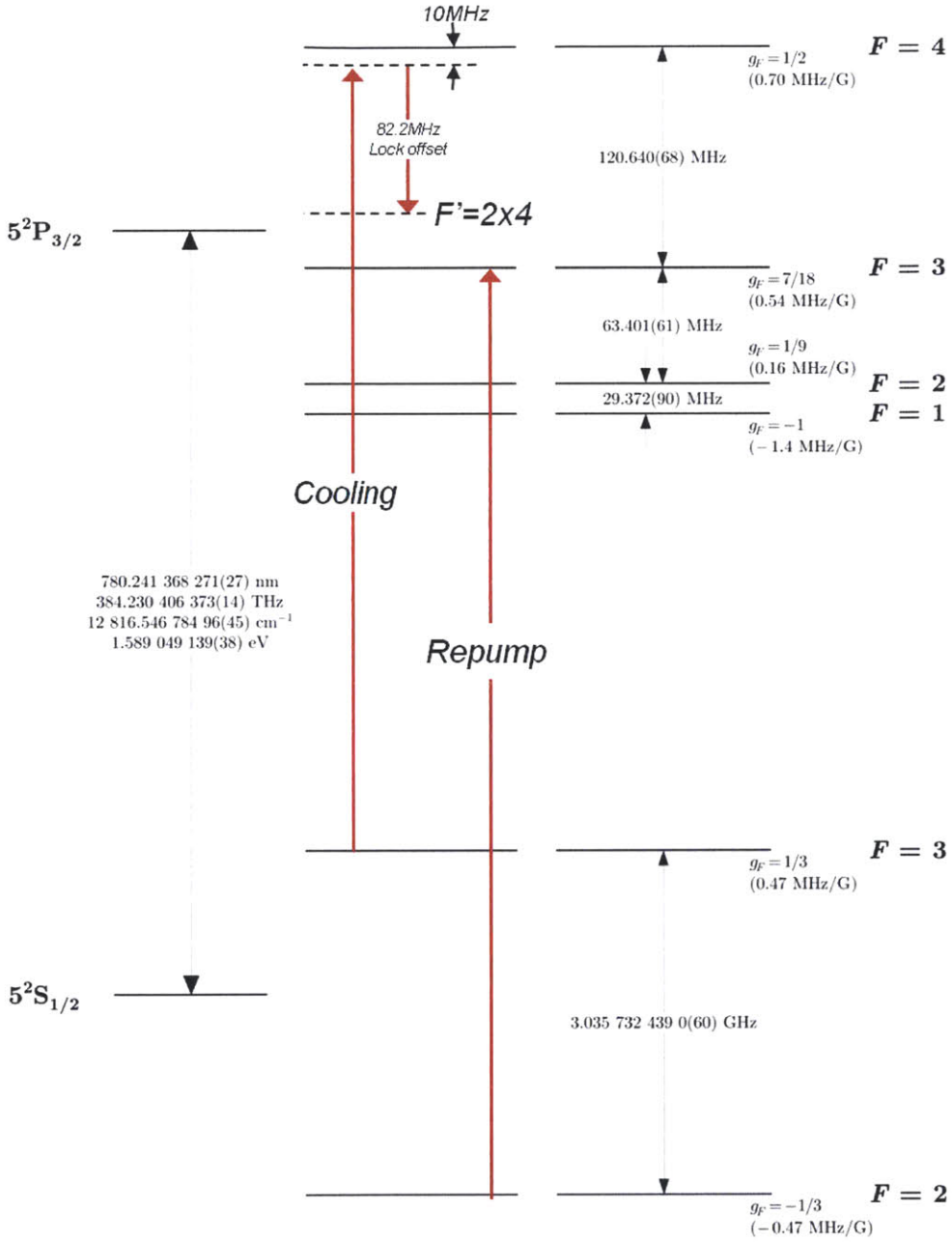

Figure 4-4: Level diagram of ^{85}Rb with laser frequencies marked. Adapted from [5]

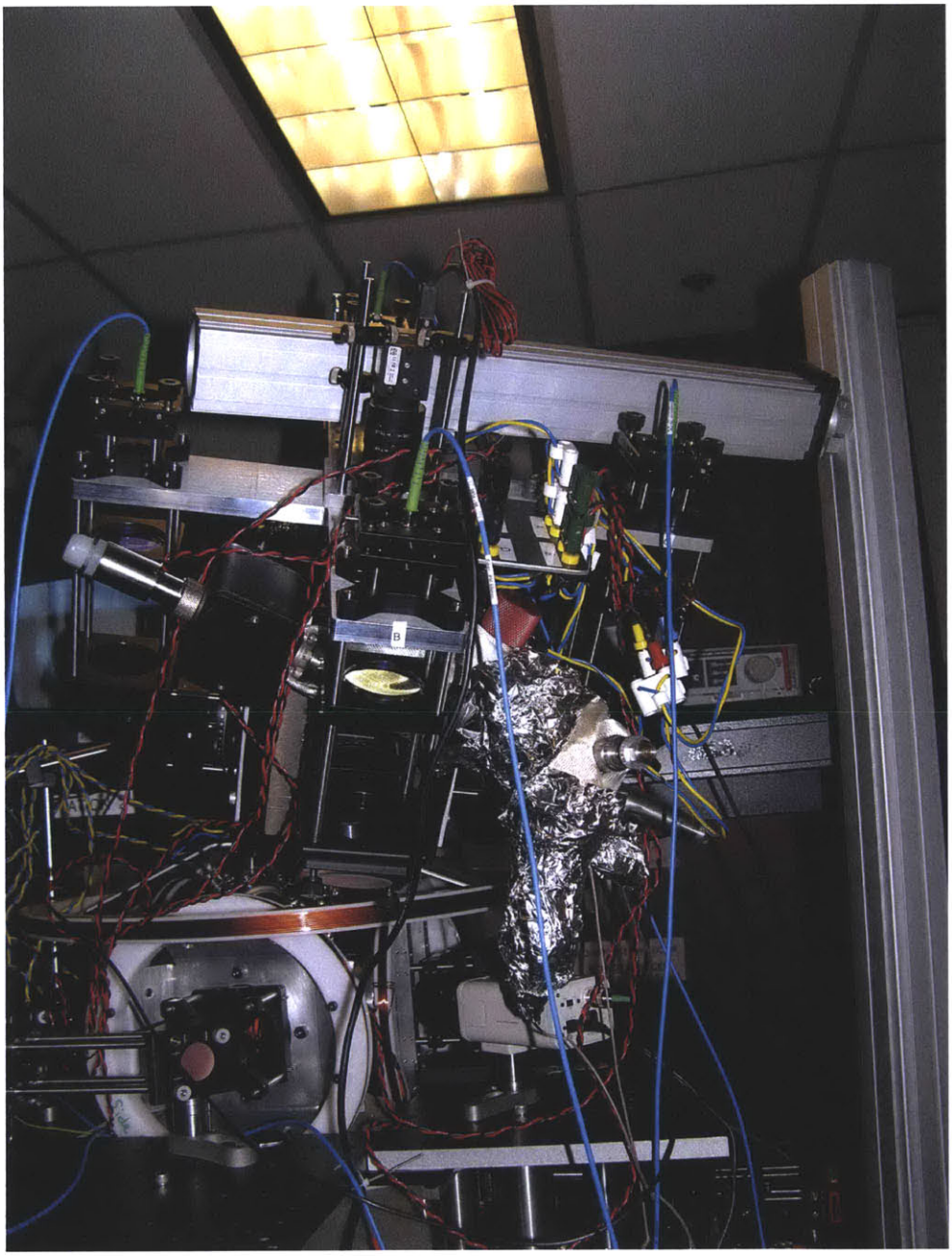

Figure 4-5: Photograph of the entire vacuum chamber from the side. Three of the four valves are visible.

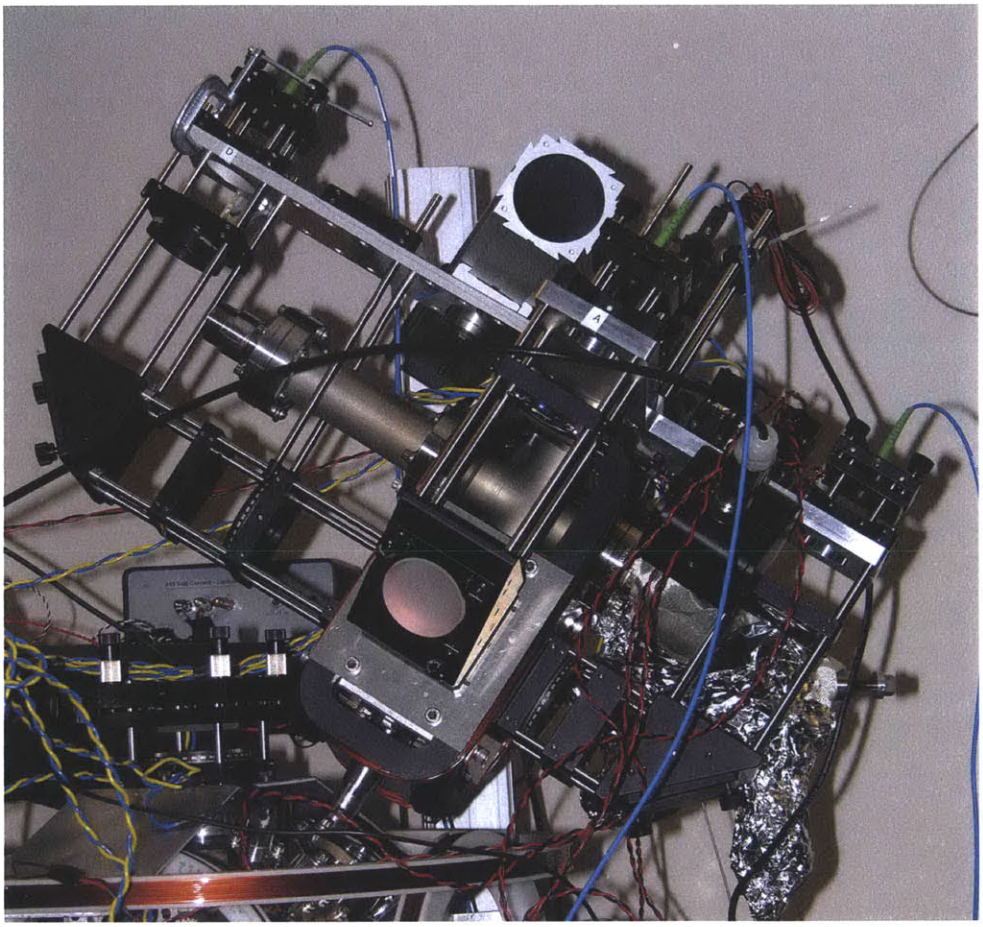

Figure 4-6: Photograph of the 2D MOT system showing the top support plate, cage-mounted optics, and side support plates. Also visible are the getter and ion pumps.

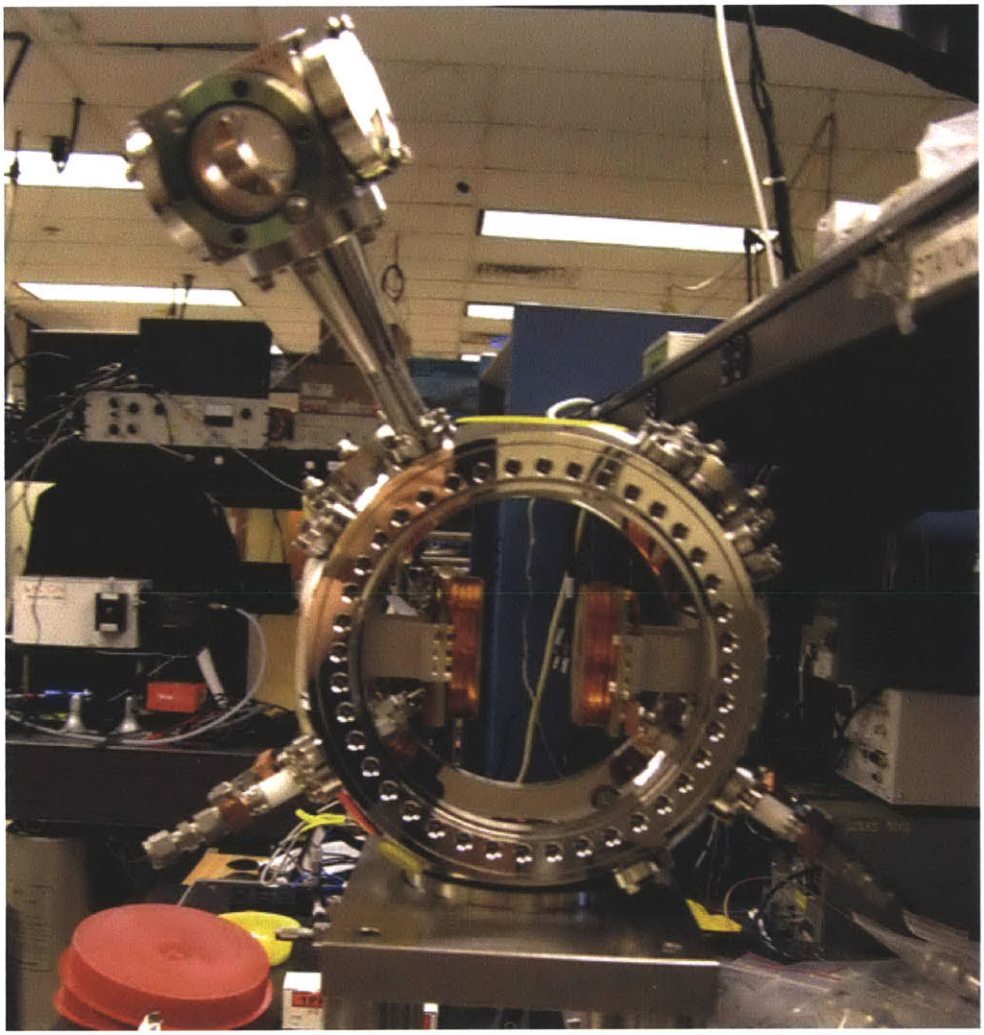

Figure 4-7: Antihelmholtz coil pair for the 3D MOT and future BEC magnetic trap.

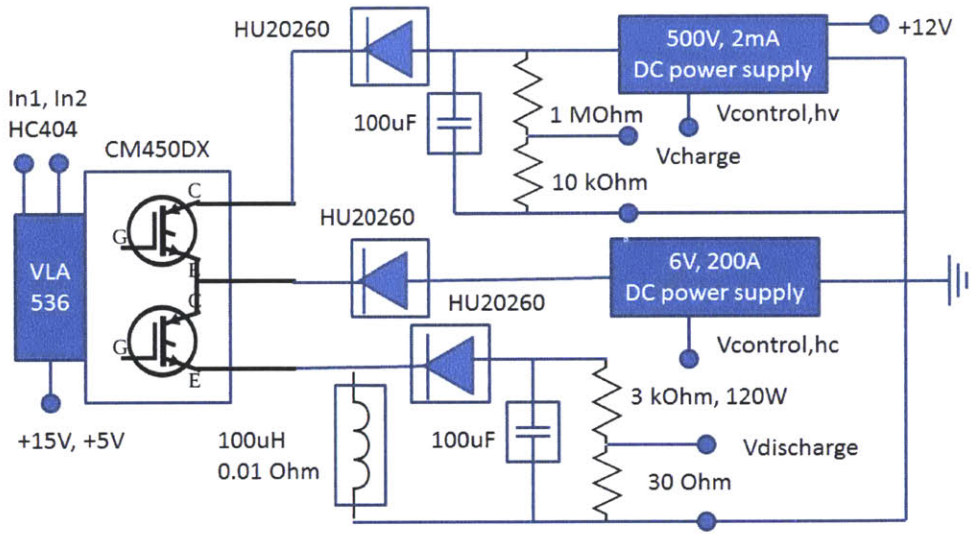

Figure 4-8: 3D MOT / magnetic trap high speed switching circuit.

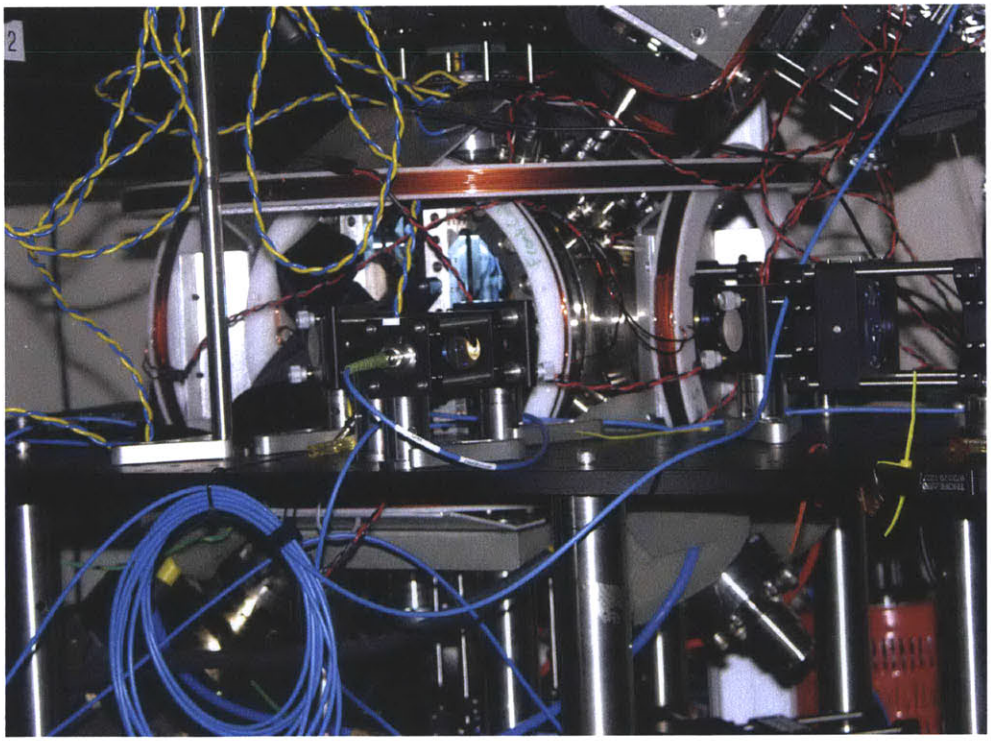

Figure 4-9: Photograph of the 3D MOT system.

THIS PAGE INTENTIONALLY LEFT BLANK

Chapter 5

Preliminary Results

The laser system is fully operational at up to 5W of total power, although it is usually operated at 2.5W. The vacuum pressure is about an order of magnitude too high for a BEC, but is adequate for early tests and will be improved after a scheduled second bake-out. We successfully created a 3D MOT and are intermittently able to load it from a 2D MOT.

5.1 Laser system results

Conversion efficiency versus input power is reported in figure 5-1. We achieve up to 5.8W of 780nm power, and the 780nm power scales quadratically in input power as expected. With careful coupling into the output fiber, up to 80% of the power is transmitted to the optics switchyard.

5.2 Vacuum system results

After 24 hours with the ion and getter pumps running, the pressure stabilizes at $4E-10$ torr in the 3D chamber and approximately $1E-7$ torr in the 2D chamber. While this is somewhat higher than the $1E-11$ torr pressure specified in section 2.2.2, we currently operate at this pressure. This decision is due in part to an upcoming relocation of RAGE to a new lab space, which will likely require another vacuum break and bake-out. We expect that a baking out for a week instead of four days would drive the pressure into the $1E-11$ torr range. In the meantime, $4E-10$ torr is more than adequate for Raman LPAI.

5.3 Cold atom results

We successfully loaded a 3D MOT from a 2D MOT. Loading from the 2D MOT was only stable for about a day before there was a failure in the RF amplifier driving the 1560nm repump modulator. We have recovered from that failure and can reliably load the 3D MOT from the backup SAES rubidium sources, as shown in figure 5-2. We are currently working to recover robust 2D to 3D MOT loading.

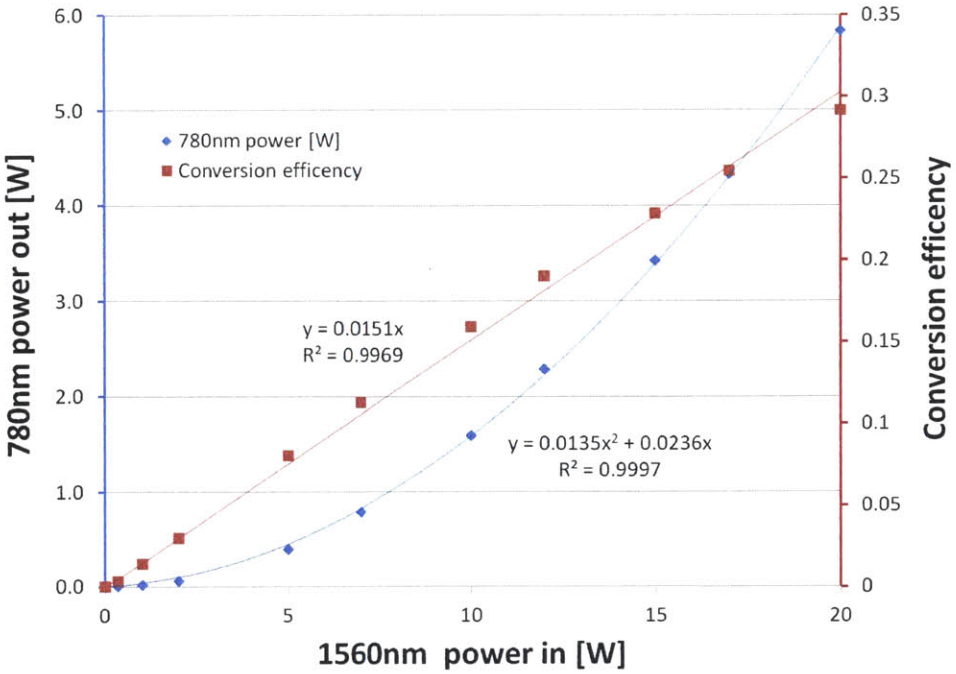

Figure 5-1: Plot of the PPLN conversion efficiency (red) and 780nm output power (blue) versus 1560nm input power. Lines are linear and quadratic fits, respectively.

Figure 5-2: CCD image of the 3D MOT, loaded from the backup SAES rubidium source. The structure to the right is one of the magnetic trap coils.

THIS PAGE INTENTIONALLY LEFT BLANK

Chapter 6

Conclusion

6.1 Summary

We successfully created a cold atom proof mass for use in high-precision Raman LPAI, and laid groundwork for future ultra-cold atom Bragg LPAI. With up to 5.8W of laser power, UHV at $4E-10$ torr, and a 3D MOT loaded from a 2D MOT, all the components are in place to begin ultra-high precision atom interferometry.

6.2 Future work

Once the 2D MOT reliability issues are resolved, we can begin doing atom interferometry and inertial sensing. The following outlines the short- and long-term goals of RAGE, as well as some ideas for the next generation of ultra-precise LPAI inertial sensors.

6.2.1 Raman LPAI

The next step is to use our MOT for Raman LPAI. This requires adding a pair of Raman beams along the z-axis of the 3D MOT. Beams will initially be retroreflected, but eventually we require independent tuning of the Raman beams: at that time, the light will be split in the switchyard to two fibers, each with a separate AOM for setting the Raman frequency. This will be done by picking off some of the light in the optics switchyard, passing it through an AOM, and overlapping it with the z-axis cooling and trapping light so it couples into the

same fiber.

Since the 3D chamber is UHV, the dwell times can be much longer than in similar Raman LPAI apparatuses and should yield significantly higher precision. We can also use RAGE as a testbed for high repetition rate Raman gravimetry using the LMT techniques reported in [32].

6.2.2 Bragg LPAI

Once RAGE has been relocated to the new lab, we will install the FORT laser system and switch from cold atom to BEC operation.

6.2.3 Long-term: integrated silicon nanophotonics

It is highly desirable to reduce the combined size, weight, area, power, and cost (SWAP-c) of any device destined for deployment, whether it be on a military vehicle or a research satellite. We have already taken a first step towards improving the ruggedness of LPAI technology by using telecom laser technology, which is robust enough to handle commercial use. In the long term, though, the next generation of RAGE must also have a significantly smaller SWAP-c footprint than the first generation device reported here.

The vacuum chamber, for example, is currently much larger than necessary. This decision was made to allow for easy optical access during the development of RAGE. Reducing the size of the vacuum chamber would reduce both the overall volume of the apparatus and the power requirements, as less power would be required for vacuum pumps and the coils could be placed much closer together and require less current.

Many of the optical components can be also shrunk significantly, but generating, modulating, locking, and delivering the light will still be a major contributor to the SWAP-c of the apparatus if we simply miniaturize the existing components. Furthermore, both free-space and fiber-coupled optics are vulnerable to noise from vibration and temperature changes. A more creative solution is necessary.

One potential solution is to leverage the fact that our system is based on telecom band light and integrate most of the optics system in a silicon nanophotonic chip. It is possible to generate, split, modulate, amplify, and convert the frequency of the light all on-chip (see

Appendix A). While 780nm light is not confined by silicon waveguides, one can envision a system where the frequency conversion happens immediately before the output. It may be possible to design a system where the only remaining free-space optics would be for collimating and circularly polarizing each beam before it reaches the vacuum chamber. Appendix A contains a paper by the author on recent advances in silicon nanophotonic technology. While Appendix A discusses work in a different wavelength regime, it is a useful demonstration of the flexibility of the silicon nanophotonic platform and provides an introduction to the topic.

Appendix B contains a paper contributed to by the author describing a method for narrowing the linewidth of a DBR laser to 300Hz. Since DBR lasers can be integrated with the silicon nanophotonic platform, the technique described in Appendix B could be used to create an ultra-narrow linewidth source within a silicon nanophotonic optics package [33]. More ambitious is the possibility of making an entire LPAI inertial sensor on a chip by combining silicon nanophotonics with BEC-on-a-chip technology pioneered by [34].

THIS PAGE INTENTIONALLY LEFT BLANK

Appendix A

Integrated Silicon Nanophotonics

The following is excerpted from reference [35]:

Demonstration of electrooptic modulation at 2165nm using a silicon Mach-Zehnder interferometer

Mackenzie A. Van Camp,[1] Solomon Assefa,[1] Douglas M. Gill,[1] Tymon Barwicz,[1] Steven M. Shank,[2] Philip M. Rice,[3] Teya Topuria,[3] and William M. J. Green[1,*]

[1]IBM T. J. Watson Research Center, 1101 Kitchawan Road, Yorktown Heights, NY 10598, USA
[2]IBM Systems & Technology Group, Microelectronics Division, 1000 River St., Essex Junction, VT 05452, USA
[3]IBM Almaden Research Center, 650 Harry Road, San Jose, CA 95120, USA
**wgreen@us.ibm.com*

Abstract: We demonstrate electrooptic modulation at a wavelength of 2165nm, using a free-carrier injection-based silicon Mach-Zehnder modulator. The modulator has a $V_\pi \cdot L$ figure of merit of 0.12V·mm, and an extinction ratio of –23dB. Optical modulation experiments are performed at bitrates up to 3Gbps. Our results illustrate that optical modulator design methodologies previously developed for telecom-band devices can be successfully applied to produce high-performance devices for a silicon nanophotonic mid-infrared integrated circuit platform.

OCIS codes: (250.7360) Waveguide modulators; (250.5300) Photonic integrated circuits.

References and links

1. R. Soref, "Mid-infrared photonics in silicon and germanium," Nat. Photonics **4**(8), 495–497 (2010).
2. R. Soref, "Silicon waveguided components for the long-wave infrared region," J. Opt. A – Pure Appl. Op. **8**(10), 840–848 (2006).
3. R. Soref, "Towards silicon-based longwave integrated optoelectronics (LIO)," SPIE Proc. **6898**, 689809, 689809-13 (2008).
4. G. Z. Mashanovich, M. M. Milošević, M. Nedeljkovic, N. Owens, B. Xiong, E. J. Teo, and Y. Hu, "Low loss silicon waveguides for the mid-infrared," Opt. Express **19**(8), 7112–7119 (2011).
5. M. M. Milošević, P. S. Matavulj, P. Y. Yang, A. Bagolini, and G. Z. Mashanovich, "Rib waveguides for mid-infrared silicon photonics," J. Opt. Soc. Am. B **26**(9), 1760–1766 (2009).
6. T. Baehr-Jones, A. Spott, R. Ilic, A. Spott, B. Penkov, W. Asher, and M. Hochberg, "Silicon-on-sapphire integrated waveguides for the mid-infrared," Opt. Express **18**(12), 12127–12135 (2010).
7. A. Spott, Y. Liu, T. Baehr-Jones, R. Ilic, and M. Hochberg, "Silicon waveguides and ring resonators at 5.5 μm," Appl. Phys. Lett. **97**(21), 213501 (2010).
8. F. Li, S. D. Jackson, C. Grillet, E. Magi, D. Hudson, S. J. Madden, Y. Moghe, C. O'Brien, A. Read, S. G. Duvall, P. Atanackovic, B. J. Eggleton, and D. J. Moss, "Low propagation loss silicon-on-sapphire waveguides for the mid-infrared," Opt. Express **19**(16), 15212–15220 (2011).
9. P. Y. Yang, S. Stankovic, J. Crnjanski, E. J. Teo, D. Thomson, A. A. Bettiol, M. B. H. Breese, W. Headley, C. Giusca, G. T. Reed, and G. Z. Mashanovich, "Silicon photonic waveguides for mid- and long-wave infrared region," J. Mater. Sci. **20**, S159–S163 (2009).
10. R. Shankar, R. Leijssen, I. Bulu, and M. Lončar, "Mid-infrared photonic crystal cavities in silicon," Opt. Express **19**(6), 5579–5586 (2011).
11. B. Kuyken, X. Liu, R. M. Osgood, Jr., R. Baets, G. Roelkens, and W. M. J. Green, "Mid-infrared to telecom-band supercontinuum generation in highly nonlinear silicon-on-insulator wire waveguides," Opt. Express **19**(21), 20172–20181 (2011).
12. R. K. W. Lau, M. Ménard, Y. Okawachi, M. A. Foster, A. C. Turner-Foster, R. Salem, M. Lipson, and A. L. Gaeta, "Continuous-wave mid-infrared frequency conversion in silicon nanowaveguides," Opt. Lett. **36**(7), 1263–1265 (2011).
13. S. Zlatanovic, J. S. Park, S. Moro, J. M. C. Boggio, I. B. Divliansky, N. Alic, S. Mookherjea, and S. Radic, "Mid-infrared wavelength conversion in silicon waveguides using ultracompact telecom-band-derived pump source," Nat. Photonics **4**(8), 561–564 (2010).
14. X. Liu, R. M. Osgood, Jr., Y. A. Vlasov, and W. M. J. Green, "Mid-infrared optical parametric amplifier using silicon nanophotonic waveguides," Nat. Photonics **4**(8), 557–560 (2010).
15. B. Kuyken, X. Liu, G. Roelkens, R. Baets, R. M. Osgood, Jr., and W. M. J. Green, "50 dB parametric on-chip gain in silicon photonic wires," Opt. Lett. **36**(22), 4401–4403 (2011).

#176325 - $15.00 USD Received 17 Sep 2012; revised 19 Nov 2012; accepted 19 Nov 2012; published 3 Dec 2012

16. N. Hattasan, A. Gassenq, L. Cerutti, J.-B. Rodriguez, E. Tournie, and G. Roelkens, "Heterogeneous integration of GaInAsSb p-i-n photodiodes on a silicon-on-insulator waveguide circuit," IEEE Photon. Technol. Lett. **23**(23), 1760–1762 (2011).
17. F. Gholami, S. Zlatanovic, E. Myslivets, S. Moro, B. P. Kuo, C. Brès, A. O. J. Wiberg, N. Alic, and S. Radic, "10Gbps parametric short-wave infrared transmitter," in *Optical Fiber Communication Conference*, OSA Technical Digest (CD) (Optical Society of America, 2011), paper OThC6.
18. N. Ophir, R. K. W. Lau, M. Menard, R. Salem, K. Padmaraju, Y. Okawachi, M. Lipson, A. L. Gaeta, and K. Bergman, "First demonstration of a 10-Gb/s RZ end-to-end four-wave-mixing based link at 1884 nm using silicon nanowaveguides," IEEE Photon. Technol. Lett. **24**(4), 276–278 (2012).
19. R. A. Soref and B. R. Bennett, "Electrooptical effects in silicon," IEEE J. Quantum Electron. **23**(1), 123–129 (1987).
20. W. M. J. Green, M. J. Rooks, L. Sekaric, and Y. A. Vlasov, "Ultra-compact, low RF power, 10 Gb/s silicon Mach-Zehnder modulator," Opt. Express **15**(25), 17106–17113 (2007).
21. Q. Xu, S. Manipatruni, B. Schmidt, J. Shakya, and M. Lipson, "12.5 Gbit/s carrier-injection-based silicon micro-ring silicon modulators," Opt. Express **15**(2), 430–436 (2007).
22. D. J. Thomson, F. Y. Gardes, J.-M. Fedeli, S. Zlatanovic, Y. Hu, B. P. P. Kuo, E. Myslivets, N. Alic, S. Radic, G. Z. Mashanovich, and G. T. Reed, "50-Gb/s silicon optical modulator," IEEE Photon. Technol. Lett. **24**(4), 234–236 (2012).
23. D. J. Thomson, F. Y. Gardes, Y. Hu, G. Mashanovich, M. Fournier, P. Grosse, J.-M. Fedeli, and G. T. Reed, "High contrast 40Gbit/s optical modulation in silicon," Opt. Express **19**(12), 11507–11516 (2011).
24. A. Brimont, D. J. Thomson, P. Sanchis, J. Herrera, F. Y. Gardes, J. M. Fedeli, G. T. Reed, and J. Martí, "High speed silicon electro-optical modulators enhanced via slow light propagation," Opt. Express **19**(21), 20876–20885 (2011).
25. J. C. Rosenberg, W. M. J. Green, S. Assefa, D. M. Gill, T. Barwicz, M. Yang, S. M. Shank, and Y. A. Vlasov, "A 25 Gbps silicon microring modulator based on an interleaved junction," Opt. Express **20**(24), 26411–26423 (2012).
26. X. Xiao, X. Li, H. Xu, Y. Hu, K. Xiong, Z. Li, T. Chu, J. Yu, and Y. Yu, "44-Gb/s silicon microring modulators based on zigzag PN junctions," IEEE Photon. Technol. Lett. **24**(19), 1712–1714 (2012).
27. H. Yu, M. Pantouvaki, J. Van Campenhout, D. Korn, K. Komorowska, P. Dumon, Y. Li, P. Verheyen, P. Absil, L. Alloatti, D. Hillerkuss, J. Leuthold, R. Baets, and W. Bogaerts, "Performance tradeoff between lateral and interdigitated doping patterns for high speed carrier-depletion based silicon modulators," Opt. Express **20**(12), 12926–12938 (2012).
28. T. Baehr-Jones, R. Ding, Y. Liu, A. Ayazi, T. Pinguet, N. C. Harris, M. Streshinsky, P. Lee, Y. Zhang, A. E.-J. Lim, T.-Y. Liow, S. H.-G. Teo, G.-Q. Lo, and M. Hochberg, "Ultralow drive voltage silicon traveling-wave modulator," Opt. Express **20**(11), 12014–12020 (2012).
29. L. Liao, A. Liu, D. Rubin, J. Basak, Y. Chetrit, H. Nguyen, R. Cohen, N. Izhaky, and M. Paniccia, "40 Gbit/s silicon optical modulator for high speed applications," Electron. Lett. **43**(22), 1196–1197 (2007).
30. M. Nedeljkovic, R. Soref, and G. Z. Mashanovich, "Free-carrier electro-refraction and electro-absorption modulation predictions for silicon over the 1-14μm infrared wavelength range," IEEE Photon. J. **3**(6), 1171–1180 (2011).
31. S. Assefa, W. M. Green, A. Rylyakov, C. Schow, F. Horst, and Y. Vlasov, "CMOS integrated nanophotonics: enabling technology for exascale computing systems," in *Optical Fiber Communication Conference*, OSA Technical Digest (CD) (Optical Society of America, 2011), paper OMM6.
32. W. M. J. Green, S. Assefa, A. Rylyakov, C. Schow, F. Horst, and Y. A. Vlasov, "CMOS integrated silicon nanophotonics: enabling technology for exascale computational systems," presented at SEMICON 2010, Chiba, Japan, 1–3 Dec. 2010.
33. T. Pinguet, S. Gloeckner, G. Masini, A. Mekis, D. J. Lockwood, and L. Pavesi, *Silicon Photonics II: Components and Integration* (Springer, 2011), Chap. 8.
34. D. Weidmann, T. Tsai, N. A. Macleod, and G. Wysocki, "Atmospheric observations of multiple molecular species using ultra-high-resolution external cavity quantum cascade laser heterodyne radiometry," Opt. Lett. **36**(11), 1951–1953 (2011).
35. K. Namjou, C. B. Roller, and P. J. McCann, "The Breathmeter: A new laser device to analyze your health," IEEE Circuits & Devices Magazine Sept/Oct, 22–28 (2006).
36. F. Capasso, R. Paiella, R. Martini, R. Colombelli, C. Gmachl, T. L. Myers, M. S. Taubman, R. M. Williams, C. G. Bethea, K. Unterrainer, H. Y. Hwang, D. L. Sivco, A. Y. Cho, A. M. Sergent, H. C. Liu, and E. A. Whittaker, "Quantum cascade lasers: Ultrahigh-speed operation, optical wireless communication, narrow linewidth, and far-infrared emission," IEEE J. Quantum Electron. **38**(6), 511–532 (2002).
37. J. Van Campenhout, W. M. J. Green, S. Assefa, and Y. A. Vlasov, "Integrated NiSi waveguide heaters for CMOS-compatible silicon thermo-optic devices," Opt. Lett. **35**(7), 1013–1015 (2010).
38. J. Van Campenhout, W. M. J. Green, S. Assefa, and Y. A. Vlasov, "Low-power, 2 x 2 silicon electro-optic switch with 110-nm bandwidth for broadband reconfigurable optical networks," Opt. Express **17**(26), 24020–24029 (2009).
39. J. Rosenberg, W. M. Green, A. Rylyakov, C. Schow, S. Assefa, B. G. Lee, C. Jahnes, and Y. Vlasov, "Ultra-low-voltage micro-ring modulator integrated with a CMOS feed-forward equalization driver," in *Optical Fiber Communication Conference*, OSA Technical Digest (CD) (Optical Society of America, 2011), paper OWQ4.

#176325 - $15.00 USD Received 17 Sep 2012; revised 19 Nov 2012; accepted 19 Nov 2012; published 3 Dec 2012

1. Introduction

The silicon-on-insulator (SOI) nanophotonic platform has been proposed as an excellent system for integrated mid-infrared (mid-IR) optical devices on account of the long-wavelength transparency of silicon and many associated CMOS-compatible materials [1–3]. Various methods have been explored for fabricating passive mid-IR waveguides and microcavities, with group-IV materials, including the use of "traditional" SOI rib and channel waveguides [4, 5], silicon-on-sapphire substrates [6–8], silicon on a porous silicon cladding [4], free-standing Si wires [9], air-clad photonic crystal membranes [10], germanium-on-silicon substrates [1–3], and hollow-core Bragg waveguides [2, 9]. Furthermore, numerous Si mid-IR components have been demonstrated, including supercontinuum sources [11], wavelength convertors [12, 13], parametric amplifiers [14, 15], and hybrid integrated GaInAsSb photodetectors [16]. While these or similar components may eventually contribute to the development of complex Si mid-IR integrated optical circuits, such systems will still likely require ultra-compact mid-IR modulators integrated on the SOI platform. To the best of our knowledge, we report here the first demonstration of mid-IR optical modulation in a silicon nanophotonic device.

Although fiber-optic transmitters using four-wave mixing to wavelength-convert a high-speed telecom-band data signal to the mid-IR [17, 18] have been demonstrated, these fiber-based systems require a number of pump lasers and high-power optical amplifiers for operation, resulting in a large and costly system. On the other hand, high index-contrast silicon nanophotonic waveguide-based electrooptic modulators using free-carrier dispersion effects [19] for external modulation have been studied extensively in telecom-band applications. Such modulators can be extremely compact, lightweight, and can provide operation at very high data rates [20–29]. Similar free-carrier electrooptic modulation approaches can certainly be applied elsewhere within the broad long-wavelength transparency window of silicon [30]. Moreover, such silicon nanophotonic modulators offer the possibility of monolithic integration with various passive optical components for mid-IR wavelength division multiplexing (WDM), as well as monolithic/hybrid integration with detectors and CMOS drive electronics [31–33], leading to single-chip mid-IR electrooptic systems. These distinct advantages make the silicon nanophotonic platform highly suitable for low-cost, deployable mid-IR integrated circuits, with applications including modulation spectroscopy [34], rapid medical diagnostics [35], and free-space communication [36].

2. Methods

The silicon nanophotonic device demonstrated here for external electrooptic modulation of a continuous-wave (CW) mid-IR optical carrier is a Mach-Zehnder interferometer (MZI), having 1 mm-long p-i-n diode phase shifters.

2.1 Device design

The MZI device shown in Fig. 1(a) is designed for use in forward bias operation using p-i-n diode phase-shifters. The phase-shifters are 1mm long, and connect at each end with passive optical 50/50 y-junction splitters. As shown in the magnified inset, a differential optical path imbalance of 85μm is included between the two arms to produce spectral interference fringes for accurate V_{π}·L measurements. The MZI has independent high-speed radio frequency (RF) signal inputs for the upper and lower arms (Signal N1/P1 and Signal N2/P2, wired to the p-i-n diode phase-shifters), and independent thermo-optic heaters (Heater 1/2) for bias point control of the electrooptic transfer function.

The MZI is assembled from a Si rib waveguide design having a central rib with nominal cross-sectional dimensions of 500x170 nm, sitting on top of a 50 nm-thick Si slab. Optical mode profile simulations are performed using the Photon Design Fimmwave mode solver, using Sellmeier models to account for the mid-IR material dispersion of the constituent silicon, silicon dioxide, and silicon nitride layers. The waveguide cross-section will be described in greater detail in Section 2.2 below. The intensity profile of the fundamental

#176325 - $15.00 USD Received 17 Sep 2012; revised 19 Nov 2012; accepted 19 Nov 2012; published 3 Dec 2012

quasi-TE guided mode, simulated at a wavelength of 2165nm, is shown in Fig. 1(b). While the waveguide dimensions are similar to those of telecom-band silicon nanophotonic devices, the mode profile and the associated modal effective index of n_{eff} = 2.016 illustrate that this design results in a single-mode waveguide with high confinement, even at longer wavelengths near 2200nm.

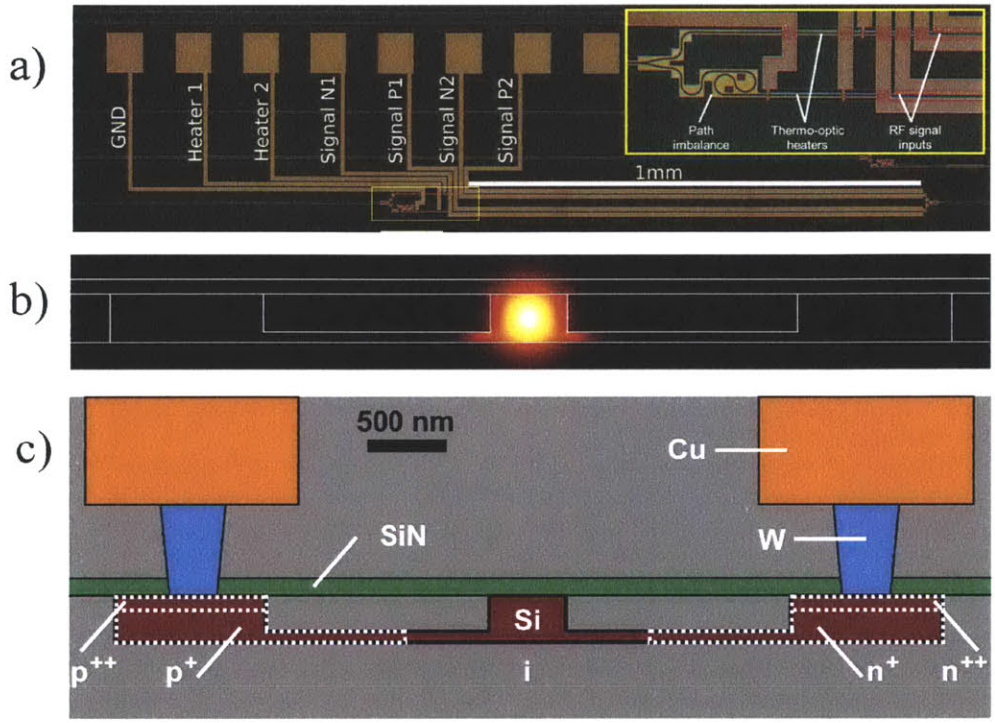

Fig. 1. a) Optical microscope image of the MZI modulator, with labels of the electrical terminal functions. Inset: Magnified detail of the 50/50 y-junction, differential optical path imbalance, thermo-optic heaters, and RF signal inputs. b) Simulated intensity profile of the fundamental quasi-TE mode at λ = 2165nm. c) Cross-section schematic of the p-i-n diode phase-shifter waveguide active region.

2.2 Device fabrication

The MZI modulator is fabricated using the IBM CMOS Silicon Nanophotonics process [31, 32], using 10 Ω·cm p-type (p ~10^{15} cm^{-3}), 200 mm-diameter SOI wafers with a 2 μm-thick buried-oxide layer and a 220 nm-thick top silicon layer. The fabrication is performed as described below, by utilizing a subset of processing modules from a standard IBM front-end CMOS process flow. An annotated schematic diagram, taken through the cross-section of the p-i-n diode phase-shifter waveguide, is shown in Fig. 1(c).

To begin, the fully-etched silicon access waveguides and partially-etched p-i-n diode rib waveguides are defined utilizing the shallow trench isolation (STI) module, using 193 nm deep-UV lithography and dry etching. Following this etch, a thick oxide layer is deposited and chemically-mechanically polished, leaving a planarized top surface.

Next, typical CMOS source/drain ion implantation and rapid thermal anneal conditions are applied to the rib waveguide to form a lateral p-i-n diode. Shallow highly doped ohmic contact regions (labeled p^{++} (boron) and n^{++} (phosphorous); impurity concentration ~10^{20} cm^{-3}) are formed at the top of the 1 μm-wide raised Si pedestals at the phase-shifter periphery. Deep p^{+} (boron) and n^{+} (phosphorous) regions (impurity concentration ~10^{19} cm^{-3}) extend from the pedestals to 500 nm away from the outer edges of the rib waveguide core.

#176325 - $15.00 USD Received 17 Sep 2012; revised 19 Nov 2012; accepted 19 Nov 2012; published 3 Dec 2012

After implant activation by a rapid thermal anneal (several seconds at a wafer temperature of approximately 1000 °C), silicide ohmic contacts are formed over the Si pedestals. Silicide formation on the waveguide core is prevented by patterning a silicon nitride (SiN) silicide-blocking layer, deposited by plasma-enhanced chemical vapor deposition (PECVD). The silicide layer on the raised pedestals is also used to form the thermal heaters for MZI bias point control [37].

Subsequently, metal contacts are formed to the active p-i-n diode waveguides and thermal heaters. A dielectric stack is deposited and planarized, and vias to the p-type and n-type contact pedestals are etched and filled with tungsten (W) plugs. Next, similar deposition, etch, and metal fill process steps are performed to form a single layer of copper (Cu) metal interconnects. Optical coupling to the Si nanophotonic chip from lensed fibers is accomplished by cleaving facets near the ends of 250 μm-long Si inverse taper mode converters.

2.3 Experimental setup

The light source used in this experiment is an IPG Photonics single-frequency external-cavity tunable Cr^{2+}:ZnSe mid-IR laser. Output from the laser is coupled into a single-mode fiber, which in turn is connected to a tapered lensed fiber for coupling light into the chip. Optical transmission through the MZI is collected through a similar lensed fiber arrangement at the chip output. Optical transmission spectra are recorded with a Yokogawa AQ6375 optical spectrum analyzer (OSA).

The p-i-n diode in one arm of the MZI is driven via a 40GHz GGB Industries Picoprobe RF probe with an externally clocked Centellax TG1B1A pattern generator. A PRBS pattern of length 2^7-1 is used. The drive signal is pre-emphasized using a one-tap equalizing RF filter as described in references [20, 21], and subsequently amplified with a Picosecond Pulse Labs 5865 12.5Gbps driver amplifier. The peak-to-peak electrical drive voltage is 1.08 V_{pp}, with 7 V_{pp} pre-emphasis at the transitions between 0 and 1 bits. An electrical DC bias of 0.3 V is applied to the p-i-n diode through a Picosecond Pulse Labs 5545 bias tee. The modulated mid-IR optical signal produced by the MZI is detected with a Discovery Semiconductor DSC-R202 long-wavelength receiver, and analyzed by an Agilent 86100A oscilloscope plug-in with 20GHz electrical bandwidth. S_{21} bandwidth measurements are taken with an Agilent E8364C PNA network analyzer.

3. Results

Various mid-IR measurements are performed to analyze the optical and electrooptic characteristics of the MZI modulator. These include recording the MZI fringe spectra at several p-i-n diode bias voltages, eyeline diagrams at modulation rates from 0.5 to 3Gbps, and S_{21} measurements of the MZI and the pre-emphasis driver.

3.1 Fringe spectra

The wavelength and bias dependence of the MZI fringes shown in Fig. 2 summarize the behavior of the device in the mid-IR. These measurements are performed with the mid-IR laser operating below threshold, where it emits broadband amplified spontaneous emission. Figure 2(a) plots the MZI transmission over a 100 nm-wide range centered at 2150nm, after normalization against the transmission through a straight, undoped on-chip reference waveguide. Three forward bias voltages are applied to the p-i-n diode phase-shifter in one arm the MZI, producing relative phase-shifts (by free-carrier dispersion) of 0 (black), $\pi/2$ (red), and π (blue).

The spectrum at 0V bias illustrates that the MZI has an insertion loss of 9.0 dB, measured at the peak of the fringe at λ = 2160nm. Ancillary measurements show that for wavelengths near 2160nm, the undoped waveguide propagation loss is 5.7 ± 0.8 dB/cm. Therefore, the majority of the MZI insertion loss originates from free-carrier absorption in the doped p-i-n diode phase-shifters, due to interaction of the guided mode's tails with the highly doped p^+

#176325 - $15.00 USD Received 17 Sep 2012; revised 19 Nov 2012; accepted 19 Nov 2012; published 3 Dec 2012

and n^+ regions. The free-carrier loss can be substantially reduced by moving the edges of the p^+ and n^+ regions further away from the Si waveguide core, and/or increasing the Si rib width for increased optical confinement at the operating wavelength of 2165nm. Altering the above structural parameters will not substantially impact the speed of a forward-biased p-i-n diode phase-shifter, in which the dominant speed limitation is imposed by the recombination lifetime of the injected free-carriers within the p-i-n junction [20, 21]. The total insertion loss through the silicon nanophotonic chip is 18.6 dB, which includes the MZI insertion loss, in addition to a net lensed-fiber-to-chip coupling loss of 9.6 ± 1 dB. On-chip silicon mode convertors specially designed to match the mid-IR mode field profile of the lensed fibers can be designed to reduce the facet coupling losses.

The decrease in peak transmission observed for increasing bias voltage is due to an imbalanced optical interference condition at the output y-junction, produced by excess free-carrier absorption within the driven p-i-n diode waveguide. This effect is general for SOI MZIs with 50-50 y-junctions and is not unique to this implementation. Furthermore, the y-junctions do not contribute significantly to the device insertion loss at 0V. The wavelength-dependent transmission loss is primarily due to increased expansion of the guided mode into the highly doped regions at longer wavelengths, with a small additional contribution from increasing long-wavelength bend losses. The MZI interference fringe contrast, however, remains large across the entire plotted spectral range, for relative phase shifts up to π.

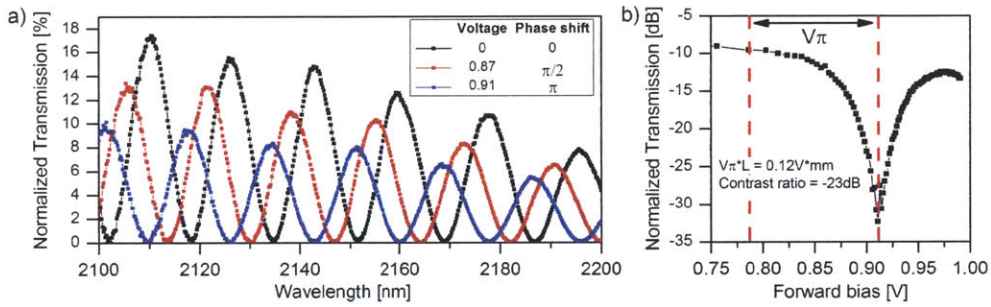

Fig. 2. Plots of normalized MZI transmission versus wavelength (a) and forward bias voltage at λ = 2160nm (b).

Figure 2(b) illustrates the dependence of the normalized transmission on forward bias voltage at 2160nm, and demonstrates over 2π of phase shift for applied single-ended voltages less than 1V. The $V_\pi \cdot L$ and fringe contrast ratio extracted from Fig. 2(b) are 0.12 V·mm and –23 dB, respectively. This is on par with previously reported performance of $V_\pi \cdot L$ = 0.06 V·mm for nanophotonic p-i-n diode MZI switches operating in the telecom band [38].

3.2 Eye diagrams

The eyeline diagrams in Fig. 3 illustrate the modulation performance of the MZI at 500Mbps, 1Gbps, 2Gbps, and 3Gbps, while modulating a CW input signal at a wavelength of 2165nm. This wavelength is chosen as a compromise between the AC-coupled optical receiver's sensitivity region (appreciable only up to 2200nm), and the above-threshold output power of the mid-IR tunable laser, which lases only at wavelengths longer than 2150nm (note that the data in Figs. 2(a)-2(b) were taken utilizing the broadband amplified spontaneous emission available at the output of the mid-IR laser when operating below threshold). Figure 2(a) shows that operation at 2165nm results in an additional 4.0dB excess modulation loss at the "1" level, relative to the insertion loss at the 2160nm fringe peak.

Directly capturing "live" eye diagrams in the mid-IR is made difficult due to a low signal-to-noise ratio, which results from the large total chip insertion losses in addition to the absence of an appropriate mid-IR optical amplifier. As a result, the detected mid-IR signal is near the combined noise floor of the receiver and oscilloscope. Therefore, the eyeline diagrams in Fig. 3 are formed by folding a 1024x averaged waveform (consisting of the entire

#176325 - $15.00 USD Received 17 Sep 2012; revised 19 Nov 2012; accepted 19 Nov 2012; published 3 Dec 2012

bit pattern) at the bit interval. Direct measurement of the eye diagram can be facilitated by reducing the facet coupling loss through the modifications suggested in Section 3.1.

The open eyes in indicate that the MZI device may be used for external optical modulation and mid-IR data transmission at bitrates up to 3Gbps. All the measurements in Fig. 3 are performed with the pre-emphasis driver optimized for bitrates near 3Gbps, resulting in the eyeline at 3Gbps in fact having the lowest level of inter-symbol interference in the center of the eye. Due to the unavailability of a DC-coupled receiver, the modulation extinction ratio is estimated from static MZI transmission spectra (similar to those in Fig. 2(a)), by comparing the 2165nm transmission at voltages corresponding to the "1" and "0" levels. This method results in an extinction ratio of 8.9dB.

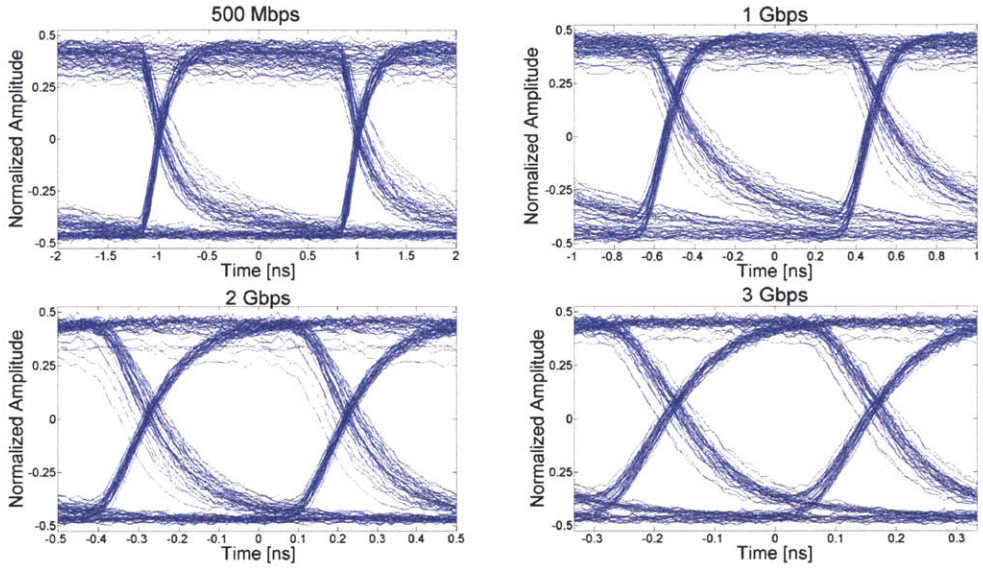

Fig. 3. Optical eyeline diagrams of a PRBS 2^7-1 bit pattern taken at 0.5Gbps, 1Gbps, 2Gbps, and 3Gbps, with pre-emphasized electrical drive. The input laser is tuned to 2165nm.

3.3 Optical S_{21}

The optical S_{21} measurements shown in Fig. 4 illustrate that the MZI device has an intrinsic 3dB rolloff at 0.4GHz, limited by the free-carrier lifetime in the p-i-n diode. The voltage S_{21} of the pre-emphasis driver described in references [20, 21] is shown in the inset. When inserted between the pattern generator and the modulator, the high-pass response of the pre-emphasis driver equalizes the MZI's low-pass characteristics, shifting the 3dB rolloff to 1.8GHz. This is consistent with operation at the 3Gbps data rate shown in Fig. 3. Improved and optimized construction of the pre-emphasis driver, or use of high-speed feed-forward equalization CMOS circuitry [39], can further increase the maximum bitrate.

#176325 - $15.00 USD Received 17 Sep 2012; revised 19 Nov 2012; accepted 19 Nov 2012; published 3 Dec 2012

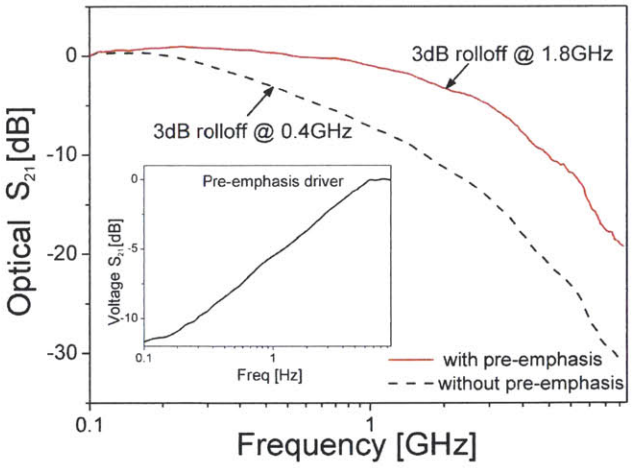

Fig. 4. Optical S_{21} of the MZI, with and without pre-emphasis. The voltage S_{21} response of the pre-emphasis electrical driver is shown in the inset.

4. Conclusion

In this report we demonstrate the first electrooptic modulation of a mid-IR signal using a silicon nanophotonic device. We achieve modulation with a bitrate of 3Gbps, an extinction ratio of −23dB, and a $V_\pi \cdot L$ figure of merit of 0.12V·mm. Nedeljkovic *et al.* [30] have predicted that interferometric free-carrier dispersion modulators can operate efficiently at wavelengths below 3000nm. The MZI electrooptic modulator demonstrated here is consistent with these predictions (up to approximately $\lambda = 2200$nm), as illustrated by the preservation of an extinction ratio greater than −20dB for large phase-shifts exceeding 2π. However, within the 3-14μm spectral range, Nedeljkovic *et al.* predict that free-carrier absorption will dominate the electrooptic phase-shift, making silicon electro-absorption modulators the preferred design configuration. Additional device research will be required to confirm these predictions.

Our results show that similar methodologies can be applied to the design and fabrication of silicon active devices operating at mid-IR wavelengths as well as in the telecom band. The performance of our MZI at 2165nm - even though it is designed with dimensions typical for telecom-band SOI devices - supports the adoption of the SOI nanophotonic platform for use in the mid-IR. Judicious optimization of the device dimensions and pre-emphasis electrical driver will further improve the optical transmission efficiency and modulation bandwidth, making this device a candidate for applications in modulation spectroscopy [34], biomedical sensing [35], and free-space communication [36].

#176325 - $15.00 USD Received 17 Sep 2012; revised 19 Nov 2012; accepted 19 Nov 2012; published 3 Dec 2012

THIS PAGE INTENTIONALLY LEFT BLANK

Appendix B

Narrow Linewidth DBR Laser

The following is excerpted from reference [36]:

Long-external-cavity distributed Bragg reflector laser with subkilohertz intrinsic linewidth

Qian Lin,[1] Mackenzie A. Van Camp,[1] Hao Zhang,[1] Branislav Jelenković,[2] and Vladan Vuletić[1,*]

[1]*Department of Physics, MIT-Harvard Center for Ultracold Atoms and Research Laboratory of Electronics, Massachusetts Institute of Technology, Cambridge, Massachusetts 02139, USA*

[2]*Institute of Physics, University of Belgrade, Serbia*

**Corresponding author: vuletic@mit.edu*

Received February 9, 2012; revised March 23, 2012; accepted March 24, 2012; posted March 27, 2012 (Doc. ID 162676); published May 30, 2012

We report on a simple, compact, and robust 780 nm distributed Bragg reflector laser with subkilohertz intrinsic linewidth. An external cavity with optical path length of 3.6 m, implemented with an optical fiber, reduces the laser frequency noise by several orders of magnitude. At frequencies above 100 kHz the frequency noise spectral density is reduced by over 33 dB, resulting in an intrinsic Lorentzian linewidth of 300 Hz. The remaining low-frequency noise is easily removed by stabilization to an external reference cavity. We further characterize the influence of feedback power and current variation on the intrinsic linewidth. The system is suitable for experiments requiring a tunable laser with narrow linewidth and low high-frequency noise, such as coherent optical communication, optical clocks, and cavity QED experiments.

OCIS codes: 140.3425, 140.2020, 140.4780.

Highly stabilized and ultranarrow-linewidth lasers are important for applications in atomic physics, quantum measurement, and quantum information science. The traditional extended-cavity diode lasers (ECDLs) [1] and distributed Bragg reflector (DBR) lasers have typical linewidths of a few hundred kilohertz to a few ten megahertz, and specially fabricated DBR lasers have achieved an intrinsic linewidth of a few kilohertz [2,3]. Optical feedback from a resonator [4] is a common approach to reduce the linewidth of an ECDL, and recent systems [5–7] have demonstrated linewidth narrowing down to 7 kHz. Other linewidth narrowing schemes, such as active electronic stabilization to a high-finesse, ultrastable vertical cavity [8,9], or an all-fiber Michelson interferometer [10], have achieved subhertz linewidth. However, due to finite loop gain at high frequencies, the high-frequency noise is usually not substantially reduced using those active stabilization methods. This may be detrimental in some applications, such as cavity sideband cooling [11,12], cavity spin squeezing [13], and other cavity QED applications [14], as well as coherent optical communication [15].

In this Letter, we present a tunable, long-external-cavity DBR laser with a 3000-fold reduction of its intrinsic linewidth to 300 Hz. This is achieved by implementing a 3.6 m long external cavity using an optical fiber. The system exhibits noise suppression of over 33 dB at frequencies of 100 kHz and above. Low-frequency noise due to mechanical or thermal fluctuations in the feedback path can be controlled by stabilizing the laser to a reference cavity using an active servo loop. Feedback-induced mode instability [16] is avoided by operating within a 13 dB wide range of feedback power.

We use a 780 nm DBR laser (Photodigm PH780DBR120T8-S) with 120 mW maximum output power as our source. The laser diode has a front facet reflectivity close to 1%, effective gain region length of 1.8 mm, and DBR reflectivity of 60% (all values are nominal values provided by manufacturer). The diode is temperature stabilized to slightly below room temperature. Throughout our measurements, we operated the laser at 100 mA (16 mW total output power). A beam splitter deflects 10% of the laser power into a 2 m long polarization-maintaining optical fiber that constitutes the feedback path (Fig. 1). An aperture is added before the angled fiber to block unwanted backreflection from the fiber tip. A mirror mounted on a piezoelectric transducer (PZT) reflects the light back into the fiber, and a quarter-wave plate in combination with a polarizing beam splitter is used to adjust the feedback power. A maximum −30 dB fractional power can be reflected back into the laser. (Henceforth we denote the fractional feedback power incident on the laser collimator as p, which may be less than the fractional power that is mode matched into the active region of the laser diode.) The external-cavity laser is set up on a 12″ × 18″ aluminum baseplate and enclosed by a plastic case to reduce environmental perturbations.

In general, the effect of external cavity optical feedback depends on the feedback power, cavity length, and the phase of the feedback light, as summarized by Tkach

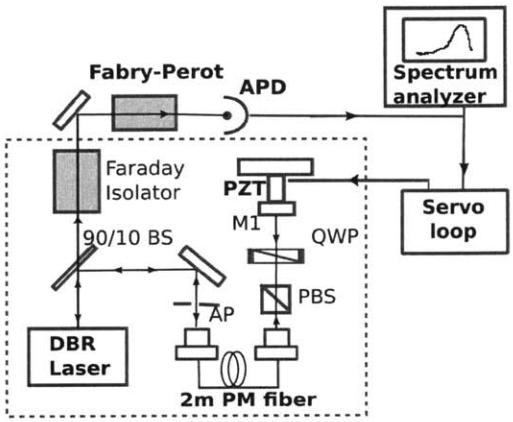

Fig. 1. Schematic setup for the long-external-cavity laser and the frequency noise characterization. M, mirror; AP, aperture; PM fiber, polarization-maintaining fiber; QWP, quarter-wave plate; BS, beam splitter; PBS, polarization beam splitter; APD, avalanche photodiode; PZT, piezoelectric transducer.

0146-9592/12/111989-03$15.00/0

and Chraplyvy [16]. Stable, narrow-linewidth operation of a DBR laser with optical feedback is only possible over a certain range of feedback power. At a fixed cavity length, three regimes of operation are observed as the fractional feedback power p is varied from −65 dB to −30 dB. The feedback phase is adjusted by moving the mirror M1 (Fig. 1) with the PZT.

- Significant line broadening is observed for $p < -64$ dB. For -64 dB $< p < -49$ dB and at certain feedback phases, the laser jumps at a rate over 1 kHz between two adjacent external cavity modes separated by 42 MHz.
- For -49 dB $< p < -40$ dB, stable single-mode operation is maintained for all feedback phases. −40 dB to −36 dB defines a transition between two regimes where multimode operation occurs occasionally but quickly converges to a single mode. Weak sidebands at adjacent external cavity modes with over 25 dB suppression from the carrier were observed.
- For -35 dB $< p < -31$ dB, intermittent multimode operation starts to appear as the feedback phase is varied, and bi-stable operation with the laser jumping slowly (<1 Hz) between nonadjacent external cavity modes separated by as much as 0.5 GHz is also observed. Nevertheless, it is still possible to maintain single-mode operation once the laser is frequency locked to some other reference, since the feedback phase is then stabilized. For $p > -31$ dB, multimode operation becomes dominant, and single-mode operation can only be achieved by increasing p from a lower level carefully while controlling the feedback phase.

To measure the laser's frequency noise spectrum, we locked the laser to the half-transmission of a Fabry–Perot cavity with a free spectral range of 1.5 GHz and linewidth of 4.0(2) MHz. The cavity transmission slope is used to convert power noise measured with a fast photodiode into frequency noise density $S_\nu(f)$. Stable locking achieved with a 15 kHz bandwidth feedback loop to the external-cavity PZT maintains a constant frequency-to-power conversion ratio. Since the lock bandwidth is low, the noise spectrum above a few ten kilohertz directly reflects the effect of optical feedback. At sufficiently high noise frequencies, $S_\nu(f)$ becomes independent of frequency with a level of S_0, corresponding to a laser emission spectrum with Lorentzian wings whose equivalent intrinsic linewidth $\Delta\nu$ can be calculated using [17]

$$\Delta\nu = \pi S_0^2. \tag{1}$$

We measured the noise spectrum from 10 kHz to 1 MHz for the long-cavity laser as well as the DBR laser without optical feedback. As shown in Fig. 2, the white noise S_0 starts at 300–400 kHz for the bare DBR laser. For the long-cavity laser with cavity length $D = 3.6$ m, suppression of over 30 dB due to optical feedback was observed for both the Lorentzian and the non-Lorentzian parts of the spectrum. A minimum intrinsic linewidth $\Delta\nu = 0.29(5)$ kHz is achieved at $p = -31$ dB, exhibiting a 3000-fold reduction in intrinsic linewidth compared to the bare laser. To verify the expected inverse quadratic dependence of $\Delta\nu$ on the external cavity length [18], we

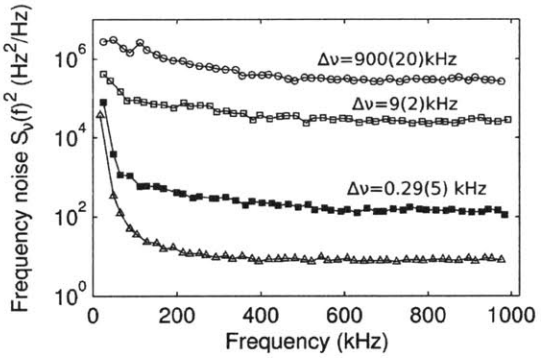

Fig. 2. Laser frequency noise spectral density for different setups. From top to bottom: bare DBR laser, short-external-cavity laser, long-external-cavity laser, and measurement noise floor. The feedback power is −31 dB for both external cavities. The white-noise level S_0 at high frequency determines the intrinsic linewidth $\Delta\nu$ according to Eq. (1).

also set up a short-external-cavity laser using the same laser with cavity length $d = 16.5(5)$ cm and operated it at the same laser current and feedback power as the long-external-cavity laser. The linewidth ratio for the two cavity lasers of $\Delta\nu_d/\Delta\nu_D = 25(1)$ dB is very close to the predicted value [18] $(D/d)^2 = 26.8(1)$ dB.

The dependence of the intrinsic linewidth $\Delta\nu$ on the fractional feedback power p at fixed current, and on a variation in current at fixed feedback power is shown in Fig. 3. In general, a higher p produces better noise suppression but makes the laser more susceptible to operating multimode. We found that for $p = -36$ dB the noise density is only 3 dB higher than the minimum value (Fig. 3), but the laser remains stable, and frequency stabilization to an external reference can be easily achieved. At fixed p and external cavity length D, the current can be tuned over a limited range (≈250 μA) while the laser remains on the same mode. For $p = -39$ dB, it is observed that when decreasing the current, $\Delta\nu$ will increase gradually until the laser jumps to an adjacent external cavity mode. On the contrary, when increasing the laser current, a flat response in $\Delta\nu$ is followed by a sudden change into multimode oscillation. Thus, as long as one locks the laser close to the center of the flat response region, a ±50 μA current change can be tolerated without significant changes in $\Delta\nu$.

To tune the laser to a target frequency, one first changes the current at fixed cavity length, corresponding to the laser jumping over adjacent external cavity modes, until the mode closest to the target frequency is reached. Then the cavity length is tuned to change the laser

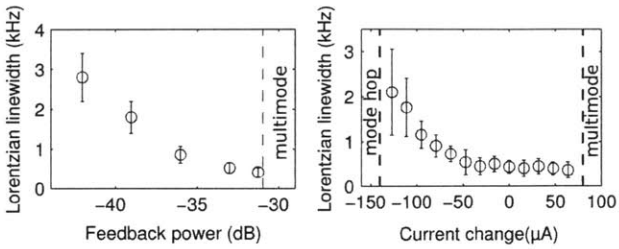

Fig. 3. The dependence of intrinsic laser linewidth $\Delta\nu$ on fractional feedback power p (left) and on laser current near the operation point at $p = -39$ dB and $I_0 = 100$ mA (right).

frequency continuously to the exact target frequency. Finally, the laser current is fine adjusted to obtain optimal linewidth narrowing. Mode-hop free tuning over 700 MHz (more than 16 external cavity modes) can also be achieved by scanning the PZT and laser current simultaneously at an appropriate ratio. This tuning range was limited by the maximum stroke of our PZT. The optimal narrowing condition can generally be maintained during the scan, but may be limited by the nonlinearity of the PZT response.

Optical feedback reduces the high-frequency noise, but servo feedback is necessary to suppress the low-frequency noise that is dominated by thermal and acoustic noise in the fiber. The free running laser exhibits a frequency stability of ≈600 kHz over 20 ms and ≈3 MHz over 1 s as measured relative to a reference laser locked to an ^{87}Rb atomic transition. To demonstrate frequency stabilization at the subkilohertz level, we locked the laser to a cavity with finesse $\mathcal{F} = 2.3(2) \times 10^4$ (linewidth $\delta\nu_c = 120(10)$ kHz) with 5 μW incident power and $p = -36$ dB using the Pound–Drever–Hall technique [19]. The feedback loop includes a low-bandwidth feedback path to the PZT and an ac coupled, high-bandwidth (2 MHz) path to the laser current. The sideband frequency is chosen at 59.2 MHz to prevent the up-converted modulation signal from triggering adjacent external cavity modes at integer multiples of 42 MHz. An rms frequency error of 0.65 (5) kHz relative to the reference cavity was calculated from the error signal in a 50 kHz bandwidth.

In conclusion, we have built a subkilohertz, tunable DBR laser in a compact long-external-cavity setup by fiber-coupling the feedback light. A 35 dB reduction in the high-frequency noise was demonstrated. Different regimes of operation under varied levels of feedback power were characterized and are in agreement with previous results [16]. We have investigated the linewidth and mode stability as a function of feedback power and laser current variation. Owing to its low cost, ease of alignment and robust performance, we believe the system can be used for a wide range of high-precision and ultra-low-noise experiments.

This work was supported in part by the National Science Foundation (NSF), the Defense Advanced Research Projects Agency (DARPA) (QuASAR), and the United States Army Research Office (ARO). Q. Lin acknowledges support from the Undergraduate Research Opportunity Program at MIT, M. A. Van Camp from the NSF IGERT program, and B. Jelenkovic from the Ministry of Education and Science of Serbia, under grant 45016.

References

1. L. Ricci, M. Weidemuller, T. Esslinger, A. Hemmerich, C. Zimmermann, V. Vuletic, W. Konig, and T. W. Hänsch, Opt. Commun. **117**, 541 (1995).
2. S. Spießberger, M. Schiemangk, A. Wicht, H. Wenzel, G. Erbert, and G. Tränkle, Appl. Phys. B **104**, 813 (2011).
3. S. Spießberger, M. Schiemangk, A. Sahm, A. Wicht, H. Wenzel, A. Peters, G. Erbert, and G. Tränkle, Opt. Express **19**, 7077 (2011).
4. B. Dahmani, L. Hollberg, and R. Drullinger, Opt. Lett. **12**, 876 (1987).
5. J. Labaziewicz, P. Richerme, K. R. Brown, I. L. Chuang, and K. Hayasaka, Opt. Lett. **32**, 572 (2007).
6. Y. Zhao, Y. Peng, T. Yang, Y. Li, Q. Wang, F. Meng, J. Cao, Z. Fang, T. Li, and E. Zang, Opt. Lett. **36**, 34 (2011).
7. K. Hayasaka, Opt. Lett. **36**, 2188 (2011).
8. A. D. Ludlow, X. Huang, M. Notcutt, T. Zanon-Willette, S. M. Foreman, M. M. Boyd, S. Blatt, and J. Ye, Opt. Lett. **32**, 641 (2007).
9. J. Alnis, A. Matveev, N. Kolachevsky, T. Udem, and T. W. Hänsch, Phys. Rev. A **77**, 053809 (2008).
10. F. Kefelian, H. Jiang, P. Lemonde, and G. Santarelli, Opt. Lett. **34**, 914 (2009).
11. K. W. Murch, K. L. Moore, S. Gupta, and D. M. Stamper-Kurn, Nat. Phys. **4**, 561 (2008).
12. M. H. Schleier-Smith, I. D. Leroux, H. Zhang, M. A. V. Camp, and V. Vuletic, Phys. Rev. Lett. **107**, 143005 (2011).
13. M. H. Schleier-Smith, I. D. Leroux, and V. Vuletic, Phys. Rev. Lett. **104**, 073604 (2010).
14. P. R. Berman, ed., *Cavity Quantum Electrodynamics (Advances in Atomic, Molecular, and Optical Physics Supplement 2)* (Academic, 1994).
15. K. Kikuchi, Electron. Lett. **23**, 885 (1987).
16. R. W. Tkach and A. R. Chraplyvy, J. Lightwave Technol. **4**, 1655 (1986).
17. D. S. Elliott, R. Roy, and S. J. Smith, Phys. Rev. A **26**, 12 (1982).
18. C. H. Henry, J. Lightwave Technol. **4**, 298 (1986).
19. R. W. P. Drever, J. L. Hall, F. V. Kowalski, J. Hough, G. M. Ford, A. J. Munley, and H. Ward, Appl. Phys. B **31**, 97 (1983).

Bibliography

[1] D. L. Butts. *Light Pulse Atom Interferometery at Short Interrogation Times for Inertial Navigation.* PhD thesis, MIT, 2012.

[2] J. Schoser, A. Bataer, R. Loew, V. Schweikhard, A. Grabowski, Y. B. Ovchinnikov, and T. Pfau. An Intense Source of Cold Rb Atoms from a Pure 2D-MOT. *ArXiv Physics e-prints*, January 2002.

[3] Covesion ppln tutorial. http://www.covesion.com/support/ppln-tutorial.html.

[4] A. Steinbach K. B. MacAdam and C. Wieman. A narrowband tunable diode laser system with grating feedback, and a saturated absorption spectrometer for cs and rb. *Am. J. Phys.*, 60:1098–1111, Dec 1992.

[5] Daniel A. Steck. Rubidium 85 d line data, Sept. 2012.

[6] Neil Barbour. Inertial components - past, present, and future. In *AIAA Guidance, Navigation and Control Conference*, pages 4290–4301, 2001.

[7] D. M. S. Johnson. *Long baseline atom interferometry.* PhD thesis, Stanford University, 2011.

[8] David L. Butts, Krish Kotru, Joseph M. Kinast, Antonije M. Radojevic, Brian P. Timmons, and Richard E. Stoner. Efficient broadband raman pulses for large-area atom interferometry. *J. Opt. Soc. Am. B*, 30(4):922–927, Apr 2013.

[9] David L. Butts, Joseph M. Kinast, Brian P. Timmons, and Richard E. Stoner. Light pulse atom interferometry at short interrogation times. *J. Opt. Soc. Am. B*, 28(3):416–421, Mar 2011.

[10] Hayden J. McGuinness, Akash V. Rakholia, and Grant W. Biedermann. High data-rate atom interferometer for measuring acceleration. *Applied Physics Letters*, 100(1):011106, 2012.

[11] S. Buchman, C.W.F. Everitt, B. Parkinson, J.P. Turneaure, and G.M. Keiser. Cryogenic gyroscopes for the relativity mission. *Physica B*, 280:497–498, 2000.

[12] C. W. F. Everitt, D. B. DeBra, B. W. Parkinson, J. P. Turneaure, J. W. Conklin, M. I. Heifetz, G. M. Keiser, A. S. Silbergleit, T. Holmes, J. Kolodziejczak, M. Al-Meshari, J. C. Mester, B. Muhlfelder, V. G. Solomonik, K. Stahl, P. W. Worden, W. Bencze, S. Buchman, B. Clarke, A. Al-Jadaan, H. Al-Jibreen, J. Li, J. A. Lipa, J. M. Lockhart, B. Al-Suwaidan, M. Taber, and S. Wang. Gravity probe b: Final results of a space experiment to test general relativity. *Phys. Rev. Lett.*, 106:221101, May 2011.

[13] T.L. Gustavson, A. Landragin, and M.A. Kasevich. Rotation sensing with a dual atom interferometer Sagnac gyroscope. *Class. Quant. Grav.*, 17:2385, 2000.

[14] Mpu-3000/mpu-3050 product specification. http://invensense.com/mems/gyro/documents/PS-MPU-3000A.pdf.

[15] D.W. Keith, C.R. Ekstrom, Q.A. Turchette, and D. Pritchard. An interferometer for atoms. *Phys. Rev. Lett.*, 66:2693, 1991.

[16] O. Carnal and J. Mlynek. Young's double-slit experiment with atoms: A simple atom interferometer. *Phys. Rev. Lett.*, 66:2689–2692, 1991.

[17] Mark Kasevich and Steven Chu. Atomic interferometry using stimulated raman transitions. *Phys. Rev. Lett.*, 67:181–184, Jul 1991.

[18] A.D. Cronin, J. Schmiedmayer, and D.E. Pritchard. Optics and interferometry with atoms and molecules. *Reviews of Modern Physics*, 81:1051–1129, 2009.

[19] J. M. McGuirk, M. J. Snadden, and M. A. Kasevich. Large area light-pulse atom interferometry. *Phys. Rev. Lett.*, 85(21):4498–4501, Nov 2000.

[20] B. Young, M.A. Kasevich, and S. Chu. *Atom Interferometry*, chapter 9, pages 363–406. Academic Press, New York, 1997.

[21] K. Moler, D.S. Weiss, M. Kasevich, and S. Chu. Theoretical analysis of velocity-selective Raman transitions. *Phys. Rev. A*, 45(1):342–348, Jan 1992.

[22] M. Kasevich and S. Chu. Measurement of the gravitational acceleration of an atom with a light-pulse atom interferometer. *Appl. Phys. B*, 54:321–332, 1992.

[23] Richard Stoner, David Butts, Joseph Kinast, and Brian Timmons. Analytical framework for dynamic light pulse atom interferometry at short interrogation times. *J. Opt. Soc. Am. B*, 28(10):2418–2429, Oct 2011.

[24] Sheng-wey Chiow, Tim Kovachy, Hui-Chun Chien, and Mark A. Kasevich. $102\hbar k$ large area atom interferometers. *Phys. Rev. Lett.*, 107:130403, Sep 2011.

[25] Holger Müller, Sheng-wey Chiow, and Steven Chu. Atom-wave diffraction between the raman-nath and the bragg regime: Effective rabi frequency, losses, and phase shifts. *Phys. Rev. A*, 77:023609, Feb 2008.

[26] Holger Müller, Sheng-wey Chiow, Quan Long, Sven Herrmann, and Steven Chu. Atom interferometry with up to 24-photon-momentum-transfer beam splitters. *Phys. Rev. Lett.*, 100:180405–180409, May 2008.

[27] E.L. Raab, M. Prentiss, A. Cable, S. Chu, and D.E. Pritchard. Trapping of neutral sodium atoms with radiation pressure. *Phys. Rev. Lett.*, 59:2631–2634, 1987.

[28] J. D. Miller, R. A. Cline, and D. J. Heinzen. Far-off-resonance optical trapping of atoms. *Phys. Rev. A*, 47:R4567–R4570, Jun 1993.

[29] K. B. Davis, M. O. Mewes, M. R. Andrews, N. J. van Druten, D. S. Durfee, D. M. Kurn, and W. Ketterle. Bose-einstein condensation in a gas of sodium atoms. *Phys. Rev. Lett.*, 75:3969–3973, Nov 1995.

[30] N. R. Newbury, C. J. Myatt, and C. E. Wieman. S wave elastic collisions between cold ground-state ^{87}Rb atoms. *Phys. Rev. A*, 51:R2680–R2683, Apr 1995.

[31] J. R. Gardner, R. A. Cline, J. D. Miller, D. J. Heinzen, H. M. J. M. Boesten, and B. J. Verhaar. Collisions of doubly spin-polarized, ultracold ^{85}Rb atoms. *Phys. Rev. Lett.*, 74:3764–3767, May 1995.

[32] Krish Kotru, David L. Butts, Joseph M. Kinast, David M. Johnson, Brian P. Timmons, Antonije M. Radojevic, and Richard E. Stoner. Atom interferometry via raman chirped adiabatic passage. In *Conference on Lasers and Electro-Optics 2012*, page QF2E.4. Optical Society of America, 2012.

[33] A.W. Fang, B.R. Koch, R. Jones, E. Lively, Di Liang, Ying hao Kuo, and J.E. Bowers. A distributed bragg reflector silicon evanescent laser. *Photonics Technology Letters, IEEE*, 20(20):1667–1669, 2008.

[34] T. W. Hnsch W. Hnsel, P. Hommelhoff and J. Reichel. Boseeinstein condensation on a microelectronic chip. *Nature*, 413:498–501, 2001.

[35] Mackenzie A. Van Camp, Solomon Assefa, Douglas M. Gill, Tymon Barwicz, Steven M. Shank, Philip M. Rice, Teya Topuria, and William M. J. Green. Demonstration of electrooptic modulation at 2165nm using a silicon mach-zehnder interferometer. *Opt. Express*, 20(27):28009–28016, Dec 2012.

[36] Qian Lin, Mackenzie A. Van Camp, Hao Zhang, Branislav Jelenković, and Vladan Vuletić. Long-external-cavity distributed bragg reflector laser with subkilohertz intrinsic linewidth. *Opt. Lett.*, 37(11):1989–1991, Jun 2012.